Journal of Physics:
Condensed Matter

PURPOSE-LED PUBLISHING™

TOPICAL REVIEW

Superconductivity in bilayer $La_3Ni_2O_7$: a review focusing on the strong-coupling Hund's rule assisted pairing mechanism

To cite this article: Zhiming Pan *et al* 2026 *J. Phys.: Condens. Matter* **38** 433002

View the article online for updates and enhancements.

You may also like

- Doping a spin-one Mott insulator: possible application to bilayer nickelate
Hanbit Oh, Hui Yang and Ya-Hui Zhang
- Effective Bi-Layer Model Hamiltonian and Density-Matrix Renormalization Group Study for the High-T_c Superconductivity in $La_3Ni_2O_7$ under High Pressure
Yang Shen, , Mingpu Qin et al.
- The Effect of Carrier Doping and Thickness on the Electronic Structures of $La_3Ni_2O_7$ Thin Films
Haoliang Shi, , Zihao Huo et al.

4-CHANNEL CONFIGURABLE OPEN RF ENGINE FOR QUANTUM EXPERIMENTS

LUGUS

Developed by Instrumentation Technologies

High bandwith arbitraty waveform generator (AWG)
Up to 1.25 GSPS

Open & programmable
Full access to FPGA implementation and firmware

Compatible with control frameworks
LabScript, ARTIQ, etc.

High power outputs
Up to 36 dBm

High-bandwidth feedback control
Open or closed-loop operation, Feedback bandwidth up to 125 MSPS

This content was downloaded from IP address 160.20.62.22 on 30/10/2026 at 13:48

Journal of Physics: Condensed Matter

Check for updates

TOPICAL REVIEW

RECEIVED
3 May 2026

REVISED
21 August 2026

ACCEPTED FOR PUBLICATION
16 September 2026

PUBLISHED
30 October 2026

Superconductivity in bilayer $La_3Ni_2O_7$: a review focusing on the strong-coupling Hund's rule assisted pairing mechanism

Zhiming Pan[1,8], **Chen Lu**[2,8], **Fan Yang**[3,*] **and Congjun Wu**[4,5,6,7,*]

[1] Department of Physics, Xiamen University, Xiamen 361005, Fujian, People's Republic of China
[2] School of Physics, Hangzhou Normal University, Hangzhou 311121, People's Republic of China
[3] School of Physics, Beijing Institute of Technology, Beijing 100081, People's Republic of China
[4] New Cornerstone science Laboratory, Department of Physics School of science, Westlake University, Hangzhou 310024, Zhejiang, People's Republic of China
[5] Institute for theoretical sciences, Westlake University, Hangzhou 310024, Zhejiang, People's Republic of China
[6] Key Laboratory for Quantum Materials of Zhejiang Province, School of science, Westlake University, Hangzhou 310024, Zhejiang, People's Republic of China
[7] Institute of Natural Sciences, Westlake Institute for Advanced Study, Hangzhou 310024, Zhejiang, People's Republic of China
[8] These two authors contributed equally to this work.
[*] Authors to whom any correspondence should be addressed.

E-mail: yangfan_blg@bit.edu.cn and wucongjun@westlake.edu.cn

Keywords: superconductivity, bilayer nickelate, unconventional superconductor, high-temperature superconductivity

Abstract

The discoveries of high-T_c superconductivity (SC) in bulk bilayer $La_3Ni_2O_7$ under pressure and of ambient-pressure SC in compressively strained thin films provide an important platform for exploring unconventional SC. Experiments reveal orbital-dependent band renormalization and sizable interlayer magnetic correlations, and show that SC emerges in association with pressure- or strain-induced structural changes. However, the role of the γ band, the symmetyr of the superconducting gap, and the microscopic pairing mechanism remain unresolved. This article reviews the relevant experimental observations and theoretical developments, with a focus on the strong-coupling Hund-assisted interlayer-pairing scenario. Within this framework, the two active Ni E_g orbitals play distinct roles. In the local strong-coupling limit, the nearly half-filled and heavily renormalized $3d_{z^2}$ orbitals experience a sizable antiferromagnetic exchange across the bilayer through the inner apical oxygen. This exchange is proposed to favor interlayer rung-singlet correlations and may produce an orbital-dependent pseudogap regime. The onsite Hund's coupling aligns the two E_g spins and generates an effective interlayer exchange between the more itinerant $3d_{x^2-y^2}$ carriers. The resulting bilayer models favor an interlayer *s*-wave state and predict that electron doping strengthens pairing. The Hund-assisted scenario can accommodate either the presence or absence of a γ pocket, provided that the $3d_{z^2}$ sector retains substantial local-moment character and sizable interlayer spin correlations. We also compare this framework with weak- and intermediate-coupling theories and other strong-coupling proposals.

1. Introduction

The discovery of high-transition-temperature (T_c) superconductivity (SC) in cuprates marked a major milestone in condensed matter physics [1]. This breakthrough has aroused considerable attention, motivating decades of research aimed at enhancing T_c and uncovering the underlying pairing mechanism [2–10]. For a long time, however, cuprates remained the unique material family known to host SC with T_c above the boiling point of liquid nitrogen. This posed a challenge to identify generic principles of unconventional high-T_c SC, is high-T_c SC uniquely tied to the specific details of copper oxides, or is it a more universal consequence of strong electronic correlations? Motivated by this, the search for nickelate analogs has been a primary focus in the community [11–20]. Nickelate series are compelling candidates since they share similar lattice structures and $3d$ electron configurations with cuprates.

© 2026 IOP Publishing Ltd. All rights, including for text and data mining, AI training, and similar technologies, are reserved.

Researchers hoped that discovering SC in nickelate systems would bridge the gap between cuprates and other strongly correlated materials, providing additional perspective to the theories of unconventional high-T_c SC.

Recently, high-T_c SC in the bilayer nickelate compound $La_3Ni_2O_7$ under high pressure has been observed [21–24]. This material family, with a high-T_c reaching approximately 80 K under pressure, establishes a novel platform for exploring strongly correlated physics. Thin films provide a complementary route to SC in bilayer nickelates. Ambient-pressure SC with onset temperatures above 40 K has been reported in epitaxial $La_3Ni_2O_7$ and $(La,Pr)_3Ni_2O_7$ films [25–30]. Experiments have further reported enhanced T_c values in rare-earth-substituted bulk samples under pressure and in thin films tuned through growth conditions or external pressure [31–33].

Extensive bulk measurements have provided deeper insights into this family of materials [34–85]. Alongside bulk studies, thin-film experiments have also rapidly progressed in recent years [86–112]. Also see the reviews [113–115]. A major advantage of superconducting thin films is that it allows the use of a broad range of experimental probes at ambient pressure, many of which are difficult to implement under high pressure. Thin films also offer greater flexibility for tuning their structural and electronic properties through growth and device design. Thin-film devices may further allow phase-sensitive tests of the superconducting order parameter.

In parallel, extensive theoretical work has addressed the correlated electronic structure and possible pairing mechanisms [116–231]. Compared with cuprates, the participation of both Ni E_g orbitals and the strong $3d_{z^2}$ interlayer coupling give bilayer nickelates a distinct low-energy structure. The pairing mechanism remains under debate, with both weak-to-intermediate-coupling theories and strong-coupling models under active study. This raises several questions.

First, what is the role of the γ band? This band is derived mainly from the $3d_{z^2}$ orbital. Angle-resolved photoemission spectroscopy (ARPES) measurements on ambient-pressure bulk samples found it below the Fermi level [40], consistent with first-principle calculations for the ambient-pressure structure [116]. Density functional theory (DFT) for the high-pressure structure instead predicts that it crosses the Fermi level and forms a γ pocket [116]. ARPES measurements on superconducting films have found the γ band either crossing the Fermi level or remaining below it, depending on the samples [91, 94, 97]. Whether the γ pocket is a general feature of the superconducting state and what role it plays in pairing remain open questions. The spectral coherence of the γ band provides additional information on the balance between itinerant quasiparticles and local-moment character in the low-energy $3d_{z^2}$ sector.

Second, how do the two E_g sectors contribute to SC? The $3d_{x^2-y^2}$ states are more itinerant, while the $3d_{z^2}$ states show stronger band renormalization and interlayer coupling. The two orbitals also hybridize and interact through onsite repulsion and Hund's coupling. Third, the pairing symmetry remains undetermined. Directional point-contact spectroscopy on pressurized bulk crystals has been interpreted as evidence for predominantly *d*-wave-like pairing, whereas high-pressure Andreev-reflection spectra favor an *s*-wave-dominant two-gap structure [66, 69]. In superconducting films, ARPES and scanning tunneling microscopy (STM) measurements report nodeless or *U*-shaped gaps on multiple bands, while terahertz spectroscopy gives a response consistent with a disorder-broadened $s_\pm$ state [93, 95, 105, 107]. The film results seem to favor a nodeless multigap state, while the relative gap signs and the interlayer character of the order parameter remain unsettled.

One theoretical framework is the strong-coupling Hund-assisted interlayer-pairing scenario [129, 167]. Related strong-coupling models have also been explored [131, 142, 169]. Within this picture, the Hund-assisted mechanism can accommodate a γ band either crossing the Fermi level or remaining below it, provided that the $3d_{z^2}$ sector retains substantial local-moment character and supports sizable interlayer spin correlations. In the strong-coupling limit, interlayer coupling through the inner apical oxygen generates AFM superexchange, which tend to favor rung-singlet correlations. Local Hund's coupling further prefers parallel alignment of the $3d_{z^2}$ and $3d_{x^2-y^2}$ spins on each Ni site. Together, the $3d_{z^2}$ interlayer exchange and local Hund's coupling generate an effective AFM exchange between the $3d_{x^2-y^2}$ spins on opposite layers. Calculations based on the resulting low-energy models favor interlayer spin-singlet pairing with extended *s*-wave symmetry. The itinerant $3d_{x^2-y^2}$ carriers provide the phase stiffness needed for global phase coherence.

The remainder of this review is organized as follows. Section 2 reviews the main experimental picture of the electronic and magnetic properties. Section 3 introduces a bilayer two-orbital Hubbard model and discusses how Hund's coupling links the spin degrees of freedom of the two orbitals. Section 4 presents a simplified t–J–$J_\perp$ model for the itinerant $3d_{x^2-y^2}$ band and discusses its interlayer pairing states. Section 5 examines the interplay between the two orbitals, including the role of $3d_{z^2}$ correlations and the proposed orbital-selective pseudogap. Section 6 compares the Hund-assisted scenario with other

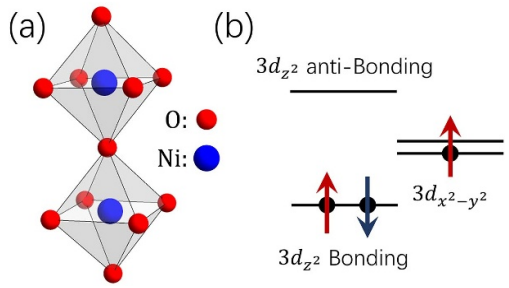


Figure 1. (a). Schematic diagram of the bilayer NiO_6 octahedral structure, illustrating the local coordination environment of the Ni ions. (b). Nominal molecular-orbital filling of the bilayer E_g states for a rung containing three electrons in the nominal ionic counting. This schematic illustrates the bonding-antibonding splitting of the $3d_{z^2}$ states. In the idealized molecular-orbital limit, the bonding state is occupied by two electrons with opposite spins, leaving the remaining electron predominantly in the in-plane $3d_{x^2-y^2}$ sector. The actual orbital occupations are modified by electronic correlations and Ni–O hybridization.

strong-coupling models and weak- to intermediate-coupling approaches. Section 7 compares bilayer nickelates with structurally related materials. Finally, section 8 summarizes the main points and discusses open questions and experiments that can distinguish among the proposed pairing scenarios.

2. Electronic properties and experiments

The local orbital structure follows from the distorted NiO_6 octahedral environment. As shown in figure 1(a), each Ni ion is coordinated by six oxygen ions [11, 21]. The dominant octahedral crystal field splits the five Ni 3*d* orbitals into a lower T_{2g} triplet and a higher E_g doublet. The E_g orbitals point toward the oxygen ligands and form strong σ-type antibonding states with the O 2*p* orbitals. The distortion of the NiO_6 octahedra further lifts the degeneracy of the two E_g orbitals.

The formal valence $Ni^{2.5+}$ corresponds to an average $3d^{7.5}$ configuration. In the ionic counting, six electrons fill the T_{2g} shell and the remaining 1.5 electrons per Ni occupy the E_g sector. The low-energy states derived from this sector contain substantial O 2*p* weight. Ni–O covalency can therefore shift the actual Ni 3*d* occupation away from its nominal value [45, 125].

The spatial orientations of the two E_g orbitals lead to different electronic dispersions. The lobes of the $3d_{x^2-y^2}$ orbital point toward the four in-plane oxygen sites. Strong *p*–*d* hybridization with the bond-oriented O $2p_{x,y}$ orbitals gives this orbital a large in-plane hopping amplitude and a broad dispersion. This in-plane Ni–O network closely resembles that of the cuprates. The main lobes of the $3d_{z^2}$ orbital extend along the *c* axis and hybridize strongly with the apical O $2p_z$ orbitals. Its in-plane dispersion is narrower, and its coupling along the bilayer direction is much stronger [40, 116, 117].

The inner apical oxygen lies between the two Ni layers and connects their $3d_{z^2}$ orbitals along a Ni–O–Ni rung. Hopping through the apical O $2p_z$ orbital generates a sizable effective interlayer hopping $t_\perp^z$ [47, 117]. After the O $2p_z$ orbital is integrated out, the two layer-resolved $3d_{z^2}$ orbitals form bonding and antibonding combinations. The lower state is bonding and the upper state is antibonding. The interlayer splitting of the $3d_{x^2-y^2}$ states is much smaller because these orbitals have little overlap with the inner apical O $2p_z$ orbital. This orbital dependence produces the large bonding-antibonding splitting in the $3d_{z^2}$ sector.

The nominal $3d^{7.5}$ configuration gives three E_g electrons on each bilayer rung. For the level ordering shown in figure 1(b), two electrons with opposite spins fill the lower $3d_{z^2}$ bonding state, and the third electron occupies a state derived mainly from $3d_{x^2-y^2}$ [117]. This molecular-orbital diagram describes the one-electron level ordering.

Local interactions modify this filling picture. The intra-orbital repulsion suppresses charge fluctuations on each Ni site, and Hund's coupling acts when the two E_g orbitals are simultaneously occupied. Ni–O covalency further redistributes charge between the Ni and oxygen orbitals. A large bonding-antibonding splitting can therefore coexist with substantial Ni-centered spin correlations in the $3d_{z^2}$ sector [124, 125]. The molecular-orbital diagram describes the single-particle splitting, whereas the correlated-rung model describes the spin and charge configurations after local interactions are included. In the lattice, the bonding $3d_{z^2}$ state acquires an in-plane dispersion and forms the predominantly $3d_{z^2}$-derived γ band [40, 116].

2.1. Structural control of superconductivity

SC in bilayer nickelates emerges under hydrostatic pressure in bulk crystals and under compressive epitaxial strain in thin film [21, 35, 89]. Both routes are associated with reduced octahedral distortions and a straighter inner-apical Ni–O–Ni bond geometry.

Bulk SC in $La_3Ni_2O_7$ is observed only within a restricted pressure range and is closely correlated with changes in crystal structure. At ambient pressure, the material crystallizes in an orthorhombic Amam structure [21]. Its low-temperature transport is sensitive to sample quality and oxygen content. High-quality stoichiometric single crystals exhibit metallic behavior at low temperatures, whereas oxygen-deficient samples can show weakly insulating transport. Under pressure, bulk $La_3Ni_2O_7$ undergoes a sequence of structural changes [21, 35]. Pressure contracts the lattice in both the in-plane and out-of-plane directions. Around 14 GPa, the lattice undergoes a transition from the *Amam* to an orthorhombic *Fmmm* phase, accompanied by a straightening of the inner-apical Ni–O–Ni bond angle from roughly 168° toward 180°. SC emerges with approximately the same pressure range. At higher pressures, a further transition to a tetragonal $I4/mmm$ structure has also been reported. The corresponding superconducting T_c reaches a maximum and then decreases with further compression [21, 35].

The occurrence of thin-film SC and its transition temperature depend strongly on the substrate and film-growth conditions. In thin films under compressive epitaxial strain, atomic-scale structural studies show that the in-plane lattice contracts while the out-of-plane Ni–O bonds along the c-axis expand [89]. Pressurized films retain a pronounced substrate dependence, and a nonsuperconducting metallic film can exhibit a similar high-symmetry local environment [89, 96, 98]. These distinct lattice responses modify the E_g bandwidths and orbital polarization while simultaneously changing the interlayer and intralayer hoppings.

Oxygen stoichiometry is an important structural factor and strongly affects SC [44]. Atomic-scale imaging of bulk crystals shows that oxygen vacancies occur primarily at inner-apical sites and are spatially inhomogeneous [45]. Inner-apical vacancies locally break the Ni–O–Ni bridge connecting the two NiO_2 planes and weaken the interlayer $3d_{z^2}$ hybridization. The superconducting response also depends on how excess oxygen is incorporated. In $La_2PrNi_2O_7$, high-pressure oxygen annealing produces an ordered interstitial-oxygen phase between neighboring bilayers, changes the carrier density, and suppresses pressure-induced SC [67]. Robust SC is associated with a nearly stoichiometric composition and an intact inner-apical oxygen network.

Rare-earth substitution provides another tuning route. Pr substitution suppresses competing Ruddlesden-Popper intergrowths and improves inner-apical oxygen occupancy, helping to stabilize nearly phase-pure $La_2PrNi_2O_7$ with bulk SC under pressure [34, 67]. Rare-earth substitution also produces an anisotropic chemical-pressure effect. Smaller rare-earth ions contract the average lattice and strengthens the orthorhombic distortion and raises the pressure required for the transition to a higher-symmetry structure [56]. Sm-substituted crystals exhibit SC onset temperatures up to 96 K, and SC is found in both monoclinic and tetragonal high-pressure structures [32].

Overall, several different routes could control SC through their combined effects on lattice structure. These results show that SC is closely tied to changes in the local structure. A structural change modifies several microscopic factors at the same time. It remains unsettled whether one of them plays the dominant role or their combined effect controls SC.

2.2. Electronic band structure

The low-energy electronic structure of bilayer $La_3Ni_2O_7$ is formed by the Ni E_g states, including the $3d_{x^2-y^2}$-dominated α and β bands and the $3d_{z^2}$-dominated γ band, as illustrated in figure 2. At ambient pressure, ARPES measurements on bulk crystals resolve an electron-like α pocket and a hole-like β pocket [40]. The hole-like β pocket provides the closest correspondence to the cuprate Fermi surface.

Structural control also tunes the low-energy electronic structure. Pressure changes both the bandwidth W and the relative energies between the two E_g orbitals. Compression generally shortens interatomic distances and enhances orbital overlap, leading to larger hopping amplitudes. The concomitant straightening of the Ni–O–Ni bond further strengthens the interlayer $3d_{z^2}$ hopping [116, 123]. The increased bandwidth raises the kinetic-energy scale and can reduce the effective correlation strength measured by U/W. Meanwhile, changes in the E_g crystal-field splitting modify the orbital polarization and redistribute low-energy spectral weight between the $3d_{x^2-y^2}$ and $3d_{z^2}$ sectors. The resulting electronic structure is therefore highly sensitive to pressure and strain, with the γ band being particularly susceptible to these changes.

The γ band originates predominantly from the bonding combination of the $3d_{z^2}$ orbitals. In ambient-pressure bulk crystals, this band is strongly renormalized and lies below the Fermi level E_F [40, 55]. For the high-pressure structure, DFT calculations predict that the γ band crosses E_F and forms an

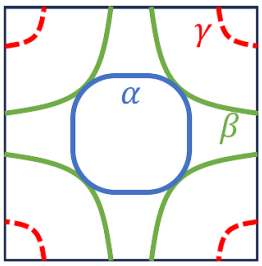


Figure 2. Schematic Fermi surfaces of bilayer $La_3Ni_2O_7$. The solid α and β sheets represent the Fermi surfaces observed by ARPES in ambient-pressure bulk samples. The dashed γ sheet denotes the additional $3d_{z^2}$-derived pocket predicted by calculations for the high-pressure structure; this pocket has not been directly measured in pressurized bulk samples.

additional Fermi-surface pocket [116, 117]. Direct ARPES measurements of the Fermi surface of pressurized bulk samples remain unavailable currently.

Superconducting bilayer nickelate films permit direct ARPES measurements at ambient pressure [91, 93, 94, 97]. The measured position of the $3d_{z^2}$-derived γ band varies among different films. ARPES measurements on superconducting ultrathin films find that the γ band crosses E_F and forms a shallow Fermi-surface pocket [30, 91, 107]. In contrast, measurements on compressively strained $La_2PrNi_2O_7$ and Sr-doped $La_3Ni_2O_7$ films place the γ band approximately 70–75 meV below E_F [94, 97]. Systematic measurements across strained and chemically substituted films find the γ-band crossing and SC over different sample ranges [94]. Photon-energy-dependent ARPES further reveals a quasi-two-dimensional dispersion of the $3d_{x^2-y^2}$-dominated bands and a finite k_z dispersion of the $3d_{z^2}$-derived band [107]. Calculations for specific thin-film and heterostructure geometries find that the position of the γ band depends sensitively on strain and structural relaxation [179].

Comparison of the measured ARPES dispersions with band-theory dispersions reveals a pronounced orbital dependence of the band renormalization. In ambient-pressure bulk crystals, the extracted renormalization factors are approximately 5–8 for γ band and about 2 for the α and β bands [40]. A strongly renormalized $3d_{z^2}$-dominated γ band is also observed in superconducting films in which it remains below E_F [94]. In Sr-doped superconducting films, the α and β bands exhibit renormalization factors of approximately 3–4 [97]. The energy position, renormalization, and out-of-plane dispersion of the γ band together characterize the degree of itinerancy of the low-energy $3d_{z^2}$ sector.

2.3. Magnetic order and spin excitations

Magnetic spectroscopy provides information on the spin dynamics and the magnetic interactions. At ambient pressure, $La_3Ni_2O_7$ develops spin-density-wave(SDW) order near 150 K. ^{139}La NMR suggests a possible double-stripe structure with moments predominantly along the c axis [48]. Neutron diffraction resolves stripe order with AFM stacking of the two NiO_2 layers within each bilayer, while muon-spin measurements show that the magnetic order extends over most of the sample volume [52].

Resonant inelastic x-ray scattering (RIXS) measurements on ambient-pressure bulk crystals resolve an optical-like magnetic mode that softens at the SDW ordering wave vector [47]. Fits based on two possible stripe configurations give interlayer exchange scale $SJ_\perp \simeq 67$–74 meV, with the fitted intralayer scales of only a few meV. Powder inelastic neutron scattering (INS) detects a weak magnetic mode near 45 meV, whose analysis within a stripe-type model gives $SJ_\perp \simeq 60$ meV and in-plane exchange scales with a few meV [53]. Single-crystal INS resolves a spin gap of about 5 meV and an out-of-plane intensity modulation with the bilayer periodicity, directly demonstrating AFM correlations between the two layers [81].

The interlayer magnetic scale is also detected and tunable by epitaxial strain. In compressively strained superconducting $La_3Ni_2O_7/SrLaAlO_4$ films, the spin-excitation bandwidth is about 10 meV larger than in ambient-pressure bulk crystals [92]. Fits performed give an interlayer exchange approximately 27% larger than the bulk value. Tensile strain reduces both the magnetic spectral weight and the fitted interlayer exchange. These measurements establish a pronounced interlayer magnetic energy scale in ambient-pressure bulk crystals and strained films, as well as its sensitivity to structural changes.

2.4. Normal-state spectral and transport anomalies

In ambient-pressure bulk crystals, ARPES reports a pseudogap-like suppression of spectral weight and a diminished quasiparticle peak near E_F in the predominantly $3d_{x^2-y^2}$-derived states [55]. Optical-conductivity measurements find a carrier kinetic energy substantially below the band-theory estimate

and a partial loss of low-frequency Drude weight below about 115 K [38]. Polarization-resolved Raman measurements reveal a symmetry-dependent redistribution of electronic spectral weight below approximately 150 K, consistent with momentum-selective gaps in the SDW state [75]. ARPES on superconducting films also finds a suppression of spectral weight near E_F that persists above T_c [107]. Ultrafast optical spectroscopy under pressure finds that the low-pressure DW-like gap is strongly suppressed as the superconducting pressure range is approached, while a distinct DW-like feature reappears above about 30 GPa [54].

In the pressure range where bulk SC occurs, the normal-state resistance is approximately linear in temperature over an extended range. At high pressures, both the coefficient of the linear term and T_c decrease gradually with increasing pressure [24]. In $La_3Ni_2O_7/LaAlO_3$ films, the low-temperature resistance evolves under modest hydrostatic pressure from an approximately Fermi-liquid form toward $R(T) - R_0 \propto T^{1.4}$ at 1.41 GPa [104]. These transport behaviors suggest possible deviations from conventional Fermi-liquid behavior.

2.5. Implications for low-energy models

The orbital-dependent band renormalization and the strongly reduced carrier kinetic energy inferred from optical conductivity show that the bare bands alone do not provide a quantitative low-energy description [38, 40]. The pronounced interlayer magnetic scale observed in bulk crystals and strained films also motivates the inclusion of explicit bilayer coupling [47, 53]. These spectral and magnetic criteria have not yet been established together in pressurized superconducting bulk samples.

First-principles calculations for candidate high-pressure structures generally find weak electron-phonon coupling and phonon-mediated transition temperatures well below the reported high-pressure values [172, 190, 193]. A phenomenological analysis of resistance data has inferred a substantially larger electron-phonon coupling [170]. The first-principles results do not support a phonon-only account of the high T_c, although the lattice contribution remains unsettled [193].

The experimental observations motivate a correlated bilayer model. The pairing interaction and the appropriate low-energy reduction remain to be determined. The low-energy role of the $3d_{z^2}$ sector depends on the property of the γ band. If a γ band below E_F is strongly renormalized and the $3d_{z^2}$ sector retains a sizable local moment together with strong interlayer spin correlations, a local-moment description with pronounced rung correlations is appropriate.

On the other hand, a shallow γ pocket with renormalized spectral weight and sizable spin response is consistent with an orbital-selective correlated metal, in which itinerant carriers coexist with fluctuating local moments and interlayer exchange [119, 123, 124]. A well-defined and strongly dispersive γ pocket with a quasiparticle weight comparable to that of the $3d_{x^2-y^2}$ bands and a weak local spin response favors an itinerant multiorbital description. This limit is considered in weak- and intermediate-coupling itinerant treatments [118, 128, 161].

The local-moment and itinerant limits can be formulated in a Ni-centered bilayer basis retaining the two E_g orbitals. In this reduction, hybridization with the O $2p$ is encoded in the Ni-centered Wannier functions and the effective hopping and crystal-field parameters, whereas ligand-hole dynamics and oxygen-defect states are not retained explicitly. The O $2p$ ligand-hole weight observed experimentally is therefore represented only indirectly [45, 47]. Explicit p–d models have been used to examine the associated charge-transfer processes [125].

3. Bilayer correlated model

We adopt a Ni-centered bilayer two-orbital Hubbard model with local Kanamori interactions, retaining the $3d_{x^2-y^2}$ and $3d_{z^2}$ orbitals on each Ni site [116, 167]. The lattice geometry and the leading hopping processes are shown in figure 3(a). The Hamiltonian is:

$$H = H_0 + H_{\mathrm{int}}.$$

Here, H_0 contains the hopping and crystal-field terms, while H_{int} describes the local Coulomb and Hund interactions. The representative lattice band structure relevant for ambient pressure is presented in figure 3(b). Depending on the filling and interaction strengths, this Hamiltonian can describe either itinerant or local-moment behavior in the $3d_{z^2}$ sector. The strong-coupling reductions discussed below apply when charge fluctuations are sufficiently suppressed and the $3d_{z^2}$ sector retains a sizable local moment.

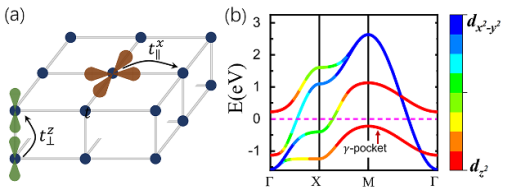


Figure 3. (a). Bilayer lattice and leading hopping amplitudes retained in equation (1). The dominant terms are the intralayer hopping $t_{\parallel}^{x}$ of the $3d_{x^2-y^2}$ orbital and the intra-bilayer hopping $t_{\perp}^{z}$ of the $3d_{z^2}$ orbital. (b). Representative bare band structure derived from the two-orbital model at ambient pressure. The horizontal dashed line denotes the Fermi level E_F. For this representative parameter set, the $3d_{z^2}$-derived γ band lies below E_F and forms no Fermi-surface pocket in the bare-band description.

Explicitly, keeping the leading hopping processes, the kinetic Hamiltonian H_0 is:

$$\begin{aligned} H_0 = & -t_{\parallel}^{x} \sum_{\langle i,j\rangle\alpha\sigma} \left(d_{x\alpha\sigma}^{\dagger}(i)\, d_{x\alpha\sigma}(j) + \text{h.c.}\right) + \Delta_g \sum_{i\alpha\sigma} d_{x\alpha\sigma}^{\dagger}(i)\, d_{x\alpha\sigma}(i) \\ & - t_{\perp}^{z} \sum_{i\sigma} \left(d_{z1\sigma}^{\dagger}(i)\, d_{z2\sigma}(i) + \text{h.c.}\right) - t_{\parallel}^{z} \sum_{\langle i,j\rangle\alpha\sigma} \left(d_{z\alpha\sigma}^{\dagger}(i)\, d_{z\alpha\sigma}(j) + \text{h.c.}\right) \\ & - \sum_{\langle i,j\rangle\alpha\sigma} t_{\parallel,j-i}^{xz} \left(d_{x\alpha\sigma}^{\dagger}(i)\, d_{z\alpha\sigma}(j) + \text{h.c.}\right). \end{aligned} \tag{1}$$

where $d_{a\alpha\sigma}^{\dagger}(i)$ creates an electron with spin σ in orbital a at site i in layer α. The orbital labels $a = x$ and $a = z$ denote the $3d_{x^2-y^2}$ and $3d_{z^2}$ orbitals, respectively. The $3d_{z^2}$ onsite energy is chosen as the reference, so that $\Delta_g = \epsilon_x - \epsilon_z$ measures the difference between the two onsite energies. An orbital-independent onsite energy is absorbed into the chemical potential, which fixes the total filling.

Within the NiO_2 planes, the larger $t_{\parallel}^{x}$ produces the strongly dispersive $3d_{x^2-y^2}$-dominated bands. In contrast, the in-plane hopping $t_{\parallel}^{z}$ for the $3d_{z^2}$ orbital is smaller because its orbital lobes point predominantly along the c-axis; nevertheless, it remains necessary to capture the slight in-plane dispersion of the $3d_{z^2}$ band. Along the c-axis, the vertical hopping $t_{\perp}^{z}$ captures the interlayer coupling of the $3d_{z^2}$ orbital within a bilayer rung. This term represents an effective Ni-Ni hopping mediated predominantly by the inner-apical O $2p_z$ orbital. A positive energy offset Δ_g raises the $3d_{x^2-y^2}$ level relative to the $3d_{z^2}$ level and therefore favors a larger $3d_{z^2}$ occupation. $t_{\parallel,j-i}^{xz}$ introduces the in-plane hybridization between the two active E_g orbitals. Because these two orbitals possess different symmetries, this interorbital hopping exhibits a strict sign alternation, satisfying $t_{\parallel,x}^{xz} = -t_{\parallel,y}^{xz} \equiv t_{\parallel}^{xz}$.

The local electron correlations are governed by the multi-orbital interaction part H_{int}, which takes the Slater-Kanamori form:

$$\begin{aligned} H_{\text{int}} = & U \sum_{ia\alpha} n_{a\alpha\uparrow}(i)\, n_{a\alpha\downarrow}(i) + V \sum_{i\alpha} n_{z\alpha}(i)\, n_{x\alpha}(i) \\ & + P \sum_{i\alpha} \left(d_{x\alpha\uparrow}^{\dagger}(i)\, d_{x\alpha\downarrow}^{\dagger}(i)\, d_{z\alpha\downarrow}(i)\, d_{z\alpha\uparrow}(i) + \text{h.c.}\right) \\ & - J_H \sum_{i\alpha} \boldsymbol{S}_{z\alpha}(i) \cdot \boldsymbol{S}_{x\alpha}(i), \end{aligned} \tag{2}$$

Here, $n_{a\alpha\sigma}(i) = d_{a\alpha\sigma}^{\dagger}(i) d_{a\alpha\sigma}(i)$ represents the number operator for an electron with spin σ in orbital a at site i in layer α. $n_{a\alpha} = n_{a\alpha\uparrow} + n_{a\alpha\downarrow}$ is the local orbital particle number and $\boldsymbol{S}_{a\alpha} = \frac{1}{2} d_{a\alpha}^{\dagger}[\boldsymbol{\sigma}] d_{a\alpha}$ is the corresponding spin operator. The interaction terms account for the intraorbital Coulomb repulsion U, interorbital repulsion V, pair-hopping amplitude P, and Hund's rule coupling J_{H}. To preserve the rotational invariance in orbital space, these parameters satisfy the Kanamori relations: $V = U - J_{\text{H}}$ and $P = J_{\text{H}}$.

Representative DFT+DMFT studies employ local interactions of approximately 3–6 eV, with the precise values depending on the correlated subspace and screening scheme [123, 124, 156]. The ratio $U/|t_{\perp}^{z}|$ provides a rough measure of the local interaction relative to the dominant hopping scale. The corresponding Hund coupling is typically 0.6–1.0 eV. Within a Ni-centered description, the relevant local charge sectors include both $3d^7$ and $3d^8$ components. Hund's coupling lowers the energy of the high-spin configurations in which both E_g orbitals are occupied and thereby affects the low-energy magnetic states.

The hopping parameters of the effective Hamiltonian are typically obtained by Wannier downfolding of first-principles band structures. As a representative bulk example, a two-orbital Wannier construction for high-pressure $La_3Ni_2O_7$ [116] gives the intralayer hopping amplitudes: $t^z_{\parallel} = 0.110$ eV, $t^{xz}_{\parallel} = 0.239$ eV, and $t^x_{\parallel} = 0.483$ eV. The interlayer $3d_{z^2}$ hopping is $t^z_{\perp} = 0.635$ eV, whereas the interlayer hopping between the $3d_{x^2-y^2}$ orbitals is negligible. The onsite energies are evaluated as $\epsilon_z = 0.409$ eV and $\epsilon_x = 0.776$ eV, maintaining a positive crystal-field splitting $\Delta_g > 0$.

Slab and epitaxial-strain calculations have extended this analysis to thin-film $La_3Ni_2O_7$ [178, 182, 184]. A common nearest-neighbor hierarchy in the bulk and thin-film Wannier descriptions is $|t^z_{\perp}| > |t^x_{\parallel}| > |t^{xz}_{\parallel}| > |t^z_{\parallel}|$ [116, 182, 184]. Realistic downfoldings retain a finite $t^z_{\parallel}$, which gives the $3d_{z^2}$ states an in-plane dispersion. In idealized minimal models, this smaller hopping is often set to zero. The numerical parameters evolve with the local structure.

3.1. Hierarchy of interactions

The low-energy physics of the two-orbital system is governed by the relative strengths of the local interaction scales. In the strong-coupling description, the dominant energy scale is the onsite Coulomb repulsion U, which suppresses intraorbital double occupancy and reduces local charge fluctuations. Virtual charge fluctuations then generate effective exchange interactions, which are often antiferromagnetic in sign. This situation would typical lead to Mott-like physics. For a $3d^8$ configuration hosting two E_g electrons, J_H aligns their spins into a local spin-1 triplet state to minimize the exchange energy.

However, the physical consequence of Hund's-driven triplet tendency is restricted by the inter-orbital Coulomb repulsion V. While J_H favors spin alignment across the two local orbitals, V imposes an energy penalty for occupying both orbitals at the same site simultaneously. This competition is of importance for determining the SC pairing mechanism. If V is artificially neglected in theoretical models, the attractive J_H channel can erroneously stabilize an unphysical on-site triplet Cooper pair. For representative parameter regime, the large magnitude of V suppresses this local pairing channel. The onsite interorbital triplet channel remains repulsive and is therefore disfavored for the parameter regime considered.

In the strong coupling limit, the magnetic interactions are highly anisotropic. Since the $3d_{z^2}$ orbitals extend along the c-axis and strongly hybridize with the shared apical oxygen $2p_z$ orbitals within a rung, they mediate a dominant interlayer AFM interaction, $J^z_{\perp}$. According to standard superexchange theory, this coupling scales as $J^z_{\perp} \sim 4(t^z_{\perp})^2/U$. In contrast, the $3d_{x^2-y^2}$ orbitals lie within the NiO_2 planes, mediating a weaker intralayer AFM exchange, $J^x_{\parallel} \sim 4(t^x_{\parallel})^2/U$. The low-energy magnetic physics is primarily governed by the strong interlayer coupling $J^z_{\perp}$, with intralayer correlations playing a secondary role.

As summarized in section 2.3, RIXS and INS measurements indicate that the interlayer magnetic exchange is substantially larger than the fitted intralayer exchange scales in ambient-pressure bulk crystals, and that strong interlayer magnetic correlations persist in compressively strained superconducting films [47, 53, 92]. This experimental hierarchy motivates treating $J^z_{\perp}$ as the leading exchange interaction in the $3d_{z^2}$ sector.

3.2. Hund assisted magnetic exchange

Motivated by the large interlayer magnetic scale discussed above, we now describe the Hund-assisted exchange mechanism in an idealized orbital-selective strong-coupling limit. The $3d_{z^2}$ sector is represented by localized spins, and the relevant $3d^8$ configurations are projected onto the onsite Hund-triplet sector. Although direct interlayer hopping for the $3d_{x^2-y^2}$ electrons is negligible, these itinerant electrons still experience a substantial effective interlayer AFM exchange, denoted as $J^x_{\perp}$. This induced interaction is primarily mediated by the on-site Hund's coupling [129, 131], as illustrated in figure 4.

Physically, this mechanism operates within each vertical rung as follows. The dominant superexchange $J^z_{\perp}$ strongly couples the localized $3d_{z^2}$ moments across the bilayer, favoring an antiparallel alignment. Concurrently, at each Ni site, the strong ferromagnetic Hund's coupling J_H favors a parallel spin alignment between the local $3d_{z^2}$ and $3d_{x^2-y^2}$ electrons. The AFM correlation established between the $3d_{z^2}$ orbitals is then transferred to the itinerant $3d_{x^2-y^2}$ orbitals. This process induces an effective interlayer AFM coupling $J^x_{\perp}$, naturally bridging the localized magnetic and the itinerant electronic sectors.

This Hund-assisted mechanism can be understood employing a semi-classical spin-coherent-state path integral approach [129]. Consider an isolated vertical rung connecting two Ni sites (labeled by the layer index $\alpha = 1, 2$) across the bilayer, as shown in figure 4. The relevant spin Hamiltonian for this single rung consists of the on-site Hund's coupling J_H and the interlayer AFM superexchange $J^z_{\perp}$ between

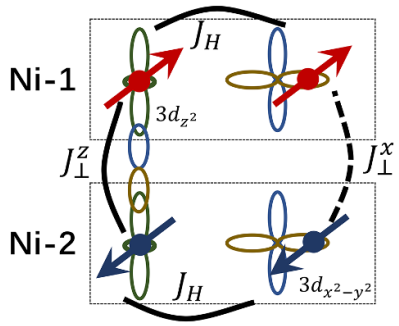


Figure 4. Schematic diagram of the effective interlayer antiferromagnetic exchange $J_\perp^x$ driven by the interplay of Hund's rule coupling and the bilayer geometry in the idealized localized strong-Hund limit. The strong superexchange $J_\perp^z$ energetically favors an antiparallel alignment of the two $3d_{z^2}$ spins across the bilayer rung. Simultaneously, the on-site ferromagnetic Hund's coupling aligns the $3d_{x^2-y^2}$ and $3d_{z^2}$ spins at each Ni sites. The antiparallel correlation of the rung $3d_{z^2}$ spins is transferred to the $3d_{x^2-y^2}$ spins, generating an effective $J_\perp^x$.

the $3d_{z^2}$ orbitals:

$$\hat{H}_{12} = -J_{\mathrm{H}} \sum_{\alpha=1,2} \boldsymbol{S}_{z,\alpha} \cdot \boldsymbol{S}_{x,\alpha} + J_\perp^z \boldsymbol{S}_{z,1} \cdot \boldsymbol{S}_{z,2} \tag{3}$$

In the path integral formalism, the quantum spin operators are mapped to classical unit vectors, $\boldsymbol{S}_{a,\alpha} \to S\hat{\Omega}_{a,\alpha}$, where $a = \{x, z\}$ is the orbital index. The resulting imaginary-time action $\mathcal{S}[\hat{\Omega}_z, \hat{\Omega}_x]$ encompasses the topological Berry phase terms, the Hund's coupling action $\mathcal{S}_{\mathrm{H}}$, and the interlayer $3d_{z^2}$ exchange $\mathcal{S}_\perp[\hat{\Omega}_z] = S^2 J_\perp^z \int_0^\beta \mathrm{d}\tau \hat{\Omega}_{z,1} \cdot \hat{\Omega}_{z,2}$.

In the idealized strong Hund's coupling regime, $J_{\mathrm{H}} \gg J_\perp^z$, the large ferromagnetic J_{H} imposes an energy penalty against local spin misalignment, forcing the electrons in the two E_{g} orbitals to form an on-site triplet state. The orientation of the $3d_{z^2}$ spin becomes tightly locked to that of the local $3d_{x^2-y^2}$ spin. This imposes a constraint on the classical unit vectors, $\hat{\Omega}_{z,\alpha}(\tau) \simeq \hat{\Omega}_{x,\alpha}(\tau)$. By integrating out the localized $3d_{z^2}$ spin degrees of freedom under this approximation, $\hat{\Omega}_{z,\alpha}$ can be effectively substituted by $\hat{\Omega}_{x,\alpha}$ in the partition function. The original interlayer action $\mathcal{S}_\perp[\hat{\Omega}_z]$ then transforms directly into an effective action for the itinerant $3d_{x^2-y^2}$ spins, $\mathcal{S}_{\mathrm{eff}}[\hat{\Omega}_x] = J_\perp^z S^2 \int_0^\beta d\tau \hat{\Omega}_{x,1} \cdot \hat{\Omega}_{x,2}$.

Under this strong-coupling constraint, the interlayer AFM correlation carried by the $3d_{z^2}$ orbitals is transferred to the $3d_{x^2-y^2}$ spins, giving rise to an effective exchange of order $J_\perp^x \approx J_\perp^z$. For finite J_{H}, the locking between the two orbital spins is incomplete, and the transferred exchange is reduced, $J_\perp^x < J_\perp^z$ [211]. Such a reduction has been considered in effective bilayer t–J models, where the transfer efficiency is treated as a finite Hund-coupling effect [201].

3.3. Effective single-orbital bilayer t–$J_\parallel$–$J_\perp$ model

The effective single-orbital model is a projected description of the dominant superconducting channel. Its reduction starts from a nearly half-filled $3d_{z^2}$ sector with suppressed charge fluctuations and sizable local moments. The dominant interlayer exchange favors rung-singlet correlations, which is hard to exhibit phase coherent. The $3d_{z^2}$ sector can be integrated out, leaving the itinerant $3d_{x^2-y^2}$ carriers as the active low-energy degrees of freedom. The influence of the $3d_{z^2}$ sector is retained through the Hund-assisted effective interlayer AFM exchange $J_\perp^x$ and the effective filling of the $3d_{x^2-y^2}$ band, which reflects the charge partition between the two E_{g} sectors.

The resulting low-energy effective physics for the superconducting channel is described by a bilayer t–$J_\parallel$–$J_\perp$ Hamiltonian [129, 131, 133]:

$$H_{\mathrm{eff}} = -t_\parallel^x \sum_{\langle i,j\rangle\alpha\sigma} \mathcal{P}\left(d_{x\alpha\sigma}^\dagger(i)\, d_{x\alpha\sigma}(j) + \mathrm{h.c.}\right)\mathcal{P} + J_\parallel^x \sum_{\langle i,j\rangle\alpha} \boldsymbol{S}_{x\alpha}(i) \cdot \boldsymbol{S}_{x\alpha}(j) + J_\perp^x \sum_i \boldsymbol{S}_{x1}(i) \cdot \boldsymbol{S}_{x2}(i) \tag{4}$$

where $\mathcal{P}$ represents the Gutzwiller projection operator. This operator enforces the strong-coupling constraint by forbidding double occupancy of the $3d_{x^2-y^2}$ orbitals at any site.

In the effective model, charge and spin dynamics operate in different spatial dimensions. The first term captures the projected kinetic energy of the itinerant $3d_{x^2-y^2}$ electrons moving within the NiO_2 planes. Their spin interactions are governed by both the intralayer AFM exchange $J_\parallel^x$ and the effective

interlayer exchange $J_\perp^x$. The direct interlayer hopping of the $3d_{x^2-y^2}$ electrons is negligible. In the projected strong-coupling limit, the onsite Hund coupling transfers the $3d_{z^2}$ rung correlation to the $3d_{x^2-y^2}$ sector. This induced interlayer exchange is the candidate interaction responsible for pairing [129].

Because the itinerant charge carriers are confined to 2D layers while the spin exchange acts in 3D, this Hamiltonian is structurally identical to the mixed-dimensional (mixD) bilayer model actively studied in ultracold atom quantum simulations [232]. Originally proposed as a highly tunable setup to realize tightly bound fermion pairs in cold gases [233–235], this mixD framework has recently been applied to analyze the pairing symmetry and BCS-Bose–Einstein condensation (BEC) crossover in bilayer nickelates [144, 148, 153, 214]. In the strong-$J_\perp$ regime, two doped carriers can lower their magnetic energy by sharing the same rung, providing a simple microscopic picture for interlayer pair formation. Upon decreasing $J_\perp/t_\parallel$, these tightly bound rung pairs evolve toward more extended BCS-like pairs, while competition with intralayer exchange can further change the dominant pairing channel. The resulting crossover and competing paired states show that even this minimal model supports rich many-body behavior, and bilayer nickelates provide a possible material setting in which such mixD pairing physics may become relevant.

Before discussing SC in the effective t–$J_\parallel$–$J_\perp$ model, we review sign-problem-free quantum Monte Carlo (QMC) results for a related bilayer Hubbard model with explicit interlayer exchange.

3.4. Sign-problem-free QMC results for a related bilayer model

Solving strongly correlated systems, specifically the Hubbard model and its variants like t–J model, remains a central challenge in condensed matter physics. A fundamental question is whether and how SC emerges upon doping the parent AFM Mott insulator. While QMC methods can rigorously solve these models at half-filling, accessing the finite-doping regime is notoriously difficult. Away from half-filling, QMC simulations are plagued by the fermion sign problem. This causes statistical errors to grow exponentially, rendering the low-temperature results computationally unreliable.

To bypass this barrier, it is desirable to construct specific models that remain sign-problem-free at finite doping. A prominent example is a class of bilayer Hubbard models designed utilizing a Kramers-invariant decomposition [205, 236]. Its bilayer geometry and explicit rung exchange make it useful for studying interlayer pairing. The sign-free construction selects a special interaction form that preserves the generalized Kramers symmetry. The resulting QMC calculations establish the many-body behavior of this model and provide a controlled reference for the nickelate problem.

The microscopic Hamiltonian of this bilayer generalized Scalapino-Zhang-Hanke (SZH) model [237], defined on a bilayer square lattice figure 5, is given by [205, 236]:

$$\begin{aligned} H = & -t_\parallel \sum_{\langle ij\rangle\sigma}\left(c_{i\sigma}^\dagger c_{j\sigma} + d_{i\sigma}^\dagger d_{j\sigma} + \text{h.c.}\right) - t_\perp \sum_{i\sigma}\left(c_{i\sigma}^\dagger d_{i\sigma} + \text{h.c.}\right) \\ & - \mu \sum_{i\sigma}\left(n_{ic\sigma} + n_{id\sigma}\right) + \frac{J_\perp}{2}\sum_i \left(S_{ic}^+ S_{id}^- + \text{h.c.}\right) + J_z \sum_i S_{ic}^z S_{id}^z \\ & + U\sum_i \left[\left(n_{ic\uparrow} - \frac{1}{2}\right)\left(n_{ic\downarrow} - \frac{1}{2}\right) + \left(n_{id\uparrow} - \frac{1}{2}\right)\left(n_{id\downarrow} - \frac{1}{2}\right)\right] \\ & + V\sum_i \left(n_{ic} - 1\right)\left(n_{id} - 1\right) \end{aligned} \tag{5}$$

Here, $c_{j\sigma}^\dagger$ ($c_{j\sigma}$) and $d_{j\sigma}^\dagger$ ($d_{j\sigma}$) denote the electron creation (annihilation) operators on site j in the upper and lower layers, respectively.

The first two terms describe the intralayer nearest-neighbor hopping ($t_\parallel$) and the vertical interlayer hopping ($t_\perp$). The interaction parameter U represents the strong on-site Hubbard repulsion, which drives the Mott physics at half-filling, while V captures the interorbital (interlayer) Coulomb repulsion across a vertical rung. The terms $J_\perp$ and J_z explicitly define the transverse and longitudinal AFM superexchange interactions between the two layers. In this model, the explicit interlayer exchange provides the interaction channel for rung-singlet pairing.

A key feature of this generalized bilayer model is that it remains free of the fermion sign problem at arbitrary doping levels over a wide region of parameter space [205, 236]. This is achieved through a Kramers-invariant decomposition framework, where the time-reversal symmetry is ensured [238]. By introducing a four-component spinor representation, $\psi_i = (c_{i\uparrow}, c_{i\downarrow}, d_{i\uparrow}, d_{i\downarrow})^T$, the Hamiltonian in

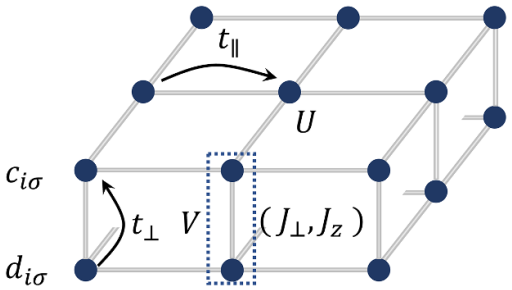


Figure 5. Schematic diagram of the generalized SZH model on a bilayer square lattice. The relevant interactions include the intralayer hopping $t_\parallel$, interlayer hopping $t_\perp$, on-site Coulomb repulsion U, interlayer Coulomb repulsion V, and interlayer AFM superexchange $(J_\perp, J_z)$.

equation (5) can be exactly mapped to a spin-$\frac{3}{2}$ fermionic Hubbard model [205, 236, 238–241]:

$$H = -t_\parallel \sum_{\langle ij \rangle} \left(\psi_i^\dagger \psi_j + \text{h.c.} \right) - t_\perp \sum_i \psi_i^\dagger \Gamma^5 \psi_i - \mu \sum_i n_i - \sum_i \frac{g_c}{2} (n_i - 2)^2 - \sum_{i,a=1-5} \frac{g_a}{2} (n_i^a)^2, \tag{6}$$

where $n_i = \psi_i^\dagger \psi_i$ is the total particle number operator, and $n_i^a = \frac{1}{2} \psi_i^\dagger \Gamma^a \psi_i$. The five Dirac matrices Γ^a $(a = 1, \cdots, 5)$ form a Clifford algebra $\{\Gamma^a, \Gamma^b\} = 2\delta_{ab}$.

The effective interaction strengths g in equation (6) are related to the original SZH parameters via:

$$\begin{aligned} 4g_c &= \frac{J_\perp}{2} + \frac{J_z}{4} - U - 3V, \\ g_{1,5} &= \frac{J_\perp}{2} + \frac{J_z}{4} - U + V, \\ g_{2,3} &= \frac{J_\perp}{2} - \frac{J_z}{4} + U - V, \\ g_4 &= -\frac{J_\perp}{2} + \frac{3J_z}{4} + U - V. \end{aligned} \tag{7}$$

In the QMC algorithm, the interaction terms are decoupled using a discrete Hubbard-Stratonovich (HS) transformation. The sign problem is avoided because this specific HS decomposition strictly preserves a generalized Kramers symmetry, denoted as $\mathcal{T}$. Physically, this $\mathcal{T}$ operator combines the standard time-reversal symmetry with a spatial layer-exchange operation. Because $\mathcal{T}$ commutes with the action for every auxiliary field configuration, the eigenvalues of the resulting fermion matrix inherently appear in complex conjugate pairs. The fermion determinant is real and strictly non-negative, providing a well-defined statistical probability weight for Monte Carlo sampling. This framework permits controlled simulations of the doped model, subject to finite-size and imaginary-time discretization limits.

Depending on the interaction parameters, the ground-state phase diagram of this bilayer model exhibits a rich variety of correlated phases, including charge-density wave, bond-current, AFM, and SC orders [205, 236, 238–241]. It provides a well-controlled platform to study the competition among these unconventional quantum states. At half-filling, the strong on-site Hubbard repulsion drives the system into a parent Mott insulating state. Depending on the spin exchange anisotropy, this insulator develops either an anisotropic Ising type or an $SU(2)$-invariant AFM order. Upon hole doping, the introduced mobile charge carriers progressively suppress the static magnetic background.

In the underdoped regime, the residual AFM background coexists with an emergent singlet superconducting phase. The QMC simulations reveal that the dominant SC pairing occurs across the vertical rungs, exhibiting an extended s-wave symmetry [236]. This numerical result suggests that the strong interlayer exchange $J_\perp$ can generate an interlayer s-wave state in a doped bilayer. Furthermore, general symmetry principles dictate a coupling among the AFM, SC, and triplet pair-density wave (tPDW) order parameters. In the coexistence region of AFM and SC, a tPDW correlation is inevitably induced as a secondary composite order.

Beyond mapping the macroscopic phase diagram, QMC simulations have systematically evaluated the parameter dependence of the SC pairing strength [205, 236]. These numerical results reveal that the on-site Hubbard interaction U exerts a distinctly non-monotonic effect on the transition temperature T_c. At low doping levels, an increasing U suppresses T_c, indicating that strong local Coulomb repulsion is detrimental when carrier mobility is highly restricted. In contrast, at higher doping levels, increasing U

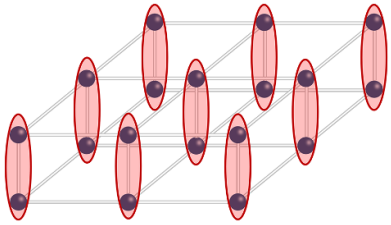


Figure 6. Schematic diagram of the interlayer *s*-wave singlet pairing in the effective bilayer model. Local singlet pairs form along the vertical rungs connecting the two layers.

significantly enhances T_c. As U increases, the optimal doping concentration shifts toward quarter-filling ($\langle n \rangle = 0.5$ per site per orbital). This value is close to the nominal $3d_{x^2-y^2}$ occupation of approximately 0.5 electron per Ni in a Ni-centered description of $La_3Ni_2O_7$.

Within the sign-free model, increasing $J_\perp$ promotes rung-pair formation, while a large bare interlayer hopping $t_\perp$ is found to inhibit macroscopic SC. A sufficiently large bare $t_\perp$ suppresses long-range SC by shifting the bonding and antibonding bands away from E_F. Under compression, both the interlayer exchange and the coherent interlayer hopping can increase. Their competing effects can produce a nonmonotonic superconducting response even when both microscopic scales grow. This trend may be relevant to the decrease of T_c observed at higher pressures and illustrates the role of the balance between coupled microscopic parameters.

Finally, exploring the normal state within this sign-problem-free model reveals anomalous transport behaviors. Calculations of the optical resistivity exhibit a linear-in-T scattering rate at elevated temperatures [205]. This temperature dependence suggests the emergence of a strange-metal phase in the bilayer system, a hallmark feature shared with correlated cuprates. The similar linear-T trend has been reported in transport measurements on pressurized $La_3Ni_2O_7$ crystals [24]. The calculated normal-state behavior is therefore consistent with the experimental transport trend, while its microscopic origin remains open.

4. Strong coupling pairing scenario

The effective single-orbital model is used to isolate the dominant superconducting channel of the itinerant $3d_{x^2-y^2}$ carriers. In the localized-rung limit, the gapped $3d_{z^2}$ fluctuations can be integrated out, with their leading effect retained in the Hund-induced interlayer exchange $J_\perp^x$. When the γ band forms a shallow pocket with small coherent weight, the full low-energy electronic structure remains two-orbital. The same t–$J_\parallel$–$J_\perp$ model can still describe the leading $3d_{x^2-y^2}$ pairing channel, provided that the $3d_{z^2}$ sector retains sizable local-spin and interlayer correlations and contributes only weakly to the coherent condensate. As the coherent γ-band weight grows and the $3d_{z^2}$ quasiparticles participate directly in pairing, a two-orbital treatment of the superconducting state becomes necessary.

In this scenario, $J_\perp^x$ provides an attractive singlet channel for $3d_{x^2-y^2}$ electrons on opposite layers, as illustrated in figure 6. Unlike the localized $3d_{z^2}$ singlets, these $3d_{x^2-y^2}$ rung-pairs are highly mobile. Because the $3d_{x^2-y^2}$ band is approximately quarter-filled, effectively placing the system deep in a heavily overdoped regime [5], the rung-pairs readily hop between neighboring in-plane sites. Their coherent motion establishes the macroscopic phase coherence required for physical SC. Since the phase stiffness is large in this heavily overdoped regime, the phase coherence temperature far exceeds the mean-field pairing temperature. Therefore, the superconducting critical temperature T_c is essentially determined by the local pairing energy scale set by $J_\perp^x$ [129].

The relative strengths of the intralayer and interlayer exchange interactions determine the competition between the two pairing channels. For the reduced model with negligible $t_\perp^x$, the limit $J_\perp^x \ll J_\parallel^x$ approaches two independent single-layer t–J models. The intralayer AFM exchange on the square lattice favors an intralayer $d_{x^2-y^2}$-wave pairing state [5, 242]. In the opposite limit, $J_\perp^x \gg J_\parallel^x$, the dominant interlayer exchange favors rung-singlet correlations. At finite doping, this regime supports strong interlayer spin-singlet pairing with A_{1g} symmetry [129, 133]. Although the real-space pair field is an interlayer A_{1g} state, it acquires opposite signs on the layer-bonding and layer-antibonding bands and therefore has an $s_\pm$ structure in the band basis.

The dimensional crossover between these *d*-wave and *s*-wave limits naturally allows an intermediate phase. When $J_\perp^x$ and $J_\parallel^x$ become comparable, both pairing components can develop. Slave-boson

mean-field (SBMF) calculations find a narrow intermediate region with $s+id$ pairing near the boundary between the intralayer d-wave and interlayer s-wave states [129]. The relative phase $\pm\pi/2$ produces a fully gapped quasiparticle spectrum in the mean-field solution. This condensation-energy gain stabilizes the complex state, which also breaks time-reversal symmetry.

The pairing tendency of the effective Hamiltonian is supported by complementary calculations [129, 131, 133]. For instance, SBMF studies [129] show that robust interlayer pairing can persist into the heavily overdoped regime, provided the interlayer superexchange $J_\perp^x$ is stronger than the intralayer $J_\parallel^x$. Beyond mean-field approximations, state-of-the-art density matrix renormalization group (DMRG) calculations [133] find dominant interlayer correlations in related parameter regimes. These results establish the internal behavior of the effective model.

The same effective Hamiltonian has also been studied in ultracold-atom quantum simulations [233–235]. In these highly tunable systems, theoretical and experimental studies of the mixD model demonstrate that mobile charges naturally pair up on the same rung to minimize magnetic energy costs [233, 234]. Recent large-scale calculations using neural quantum states identified robust SC over a wide range of doping [214].

4.1. Interlayer *s*-wave pairing

To address the strong local correlations in the $3d_{x^2-y^2}$ band, the effective bilayer t–$J_\parallel$–$J_\perp$ model in equation (4) is analyzed within the SBMF framework [5, 242]. This approach fractionalizes the physical electron into a neutral spin-1/2 fermion (spinon) $f_{i\alpha\sigma}^\dagger$, and a spinless charged boson (holon) $b_{i\alpha}$. The physical electron creation operator at site i is thus expressed as $d_{x\alpha\sigma}^\dagger(i) = f_{i\alpha\sigma}^\dagger b_{i\alpha}$. This representation naturally enforces the Gutzwiller constraint, which forbids double occupancy on any given site, through the local condition $\sum_\sigma f_{i\alpha\sigma}^\dagger f_{i\alpha\sigma} + b_{i\alpha}^\dagger b_{i\alpha} = 1$.

At sufficiently low temperatures, the bosonic holons are assumed to undergo BEC, forming a coherent macroscopic background with an expectation value $b_{i\alpha} = \sqrt{\delta}$, where $\delta = 1-2x$ denotes the hole-doping concentration from half-filled. Once the charge degree of freedom condenses, the low-energy physics is governed entirely by the spinon dynamics.

By decoupling the superexchange interactions via the standard mean-field approximation [5, 242], the spinon dynamics are characterized by the intralayer and interlayer spinon expectation values:

$$\begin{aligned}
\chi_{ij}^{(\alpha)} &= \langle f_{j\alpha\uparrow}^\dagger f_{i\alpha\uparrow} + f_{j\alpha\downarrow}^\dagger f_{i\alpha\downarrow}\rangle \equiv \chi_{j-i}^{(\alpha)},\\
\Delta_{ij}^{(\alpha)} &= \langle f_{j\alpha\downarrow} f_{i\alpha\uparrow} - f_{j\alpha\uparrow} f_{i\alpha\downarrow}\rangle \equiv \Delta_{j-i}^{(\alpha)},\\
\chi_{i,\perp} &= \langle f_{i2\uparrow}^\dagger f_{i1\uparrow} + f_{i2\downarrow}^\dagger f_{i1\downarrow}\rangle \equiv \chi_z,\\
\Delta_{i,\perp} &= \langle f_{i2\downarrow} f_{i1\uparrow} - f_{i2\uparrow} f_{i1\downarrow}\rangle \equiv \Delta_z.
\end{aligned} \tag{8}$$

Here, $\chi_{ij}^{(\alpha)}$ and χ_z denote the in-plane and vertical rung spinon hopping parameters, respectively, while $\Delta_{ij}^{(\alpha)}$ and Δ_z represent the corresponding spinon pairing amplitudes.

Within the SBMF theory, the realization of a macroscopic superconducting state requires both the BEC of the holons and the coherent Cooper pairing of the spinons. The physical superconducting order parameter is therefore defined as a composite quantity $\tilde{\Delta}_{\rm SC} = \delta\Delta_{\rm pair}$, where δ is the condensed holon density and $\Delta_{\rm pair}$ is the relevant spinon pairing amplitude defined in equation (8).

Self-consistent solutions of the mean-field Hamiltonian yield a ground-state phase diagram governed primarily by the electron filling fraction x and the magnetic interaction ratio $J_\perp^x/J_\parallel^x$ [129]. As this ratio increases, the system undergoes a dimensional crossover across three distinct superconducting phases. For weak interlayer coupling and fillings proximity to half-filling, the system favors a standard intralayer d-wave pairing, analogous to the well-established physics of single-layer cuprates. Conversely, when the interlayer superexchange dominates ($J_\perp^x > J_\parallel^x$), the formation of robust vertical rung singlets drives the system into an interlayer s-wave pairing state. Separating these two limits is a narrow intermediate phase with a mixed $s+id$ pairing symmetry. This phase spontaneously breaks time-reversal symmetry, smoothly mediating the crossover between the strictly two-dimensional d-wave regime and the strongly coupled bilayer s-wave regime.

The calculated superconducting order parameter $\tilde{\Delta}_{\rm SC}$ is plotted in figure 7(a) as a function of the electron filling level x for various exchange ratios $J_\perp^x/J_\parallel^x$ [129]. Across all evaluated ratios, $\tilde{\Delta}_{\rm SC}$ increases monotonically with x. To understand this trend, recall that the system is situated in a heavily overdoped regime characterized by a large holon density δ. Since the electron filling x and the hole doping δ are inversely related ($\delta = 1-2x$), increasing x effectively brings the system closer to the optimal doping regime. This behavior aligns with the well-known physics of the single-layer t–J model for cuprates.

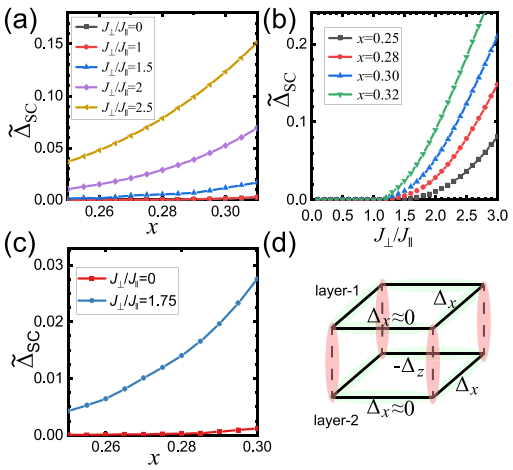


Figure 7. (a). Ground-state superconducting order parameter $\tilde{\Delta}_{SC}$ as a function of the filling fraction x at $J_\parallel^x = 0.4t_\parallel^x$ for various coupling ratios $J_\perp^x/J_\parallel^x = 0, 1, 1.5, 2, 2.5$, obtained from slave-boson mean-field calculations. (b). calculated $\tilde{\Delta}_{SC}$ versus $J_\perp^x/J_\parallel^x$ for $x = 0.25, 0.28, 0.3, 0.32$. (c). Comparison of $\tilde{\Delta}_{SC}$ versus x between the decoupled layer limit $J_\perp^x/J_\parallel^x = 0$ and the physically relevant coupled bilayer regime $J_\perp^x/J_\parallel^x = 1.75$. (d). Pairing configuration of the emergent interlayer s-wave state at $J_\perp^x/J_\parallel^x = 1.75$. Reprinted (figure) with permission from [129], Copyright (2024) by the American Physical Society.

For instance, in the decoupled limit $J_\perp^x = 0$, $\tilde{\Delta}_{SC}$ drops rapidly as the system approaches quarter-filling ($x \to 0.25$, corresponding to $\delta \to 0.5$), reflecting a significant deviation from optimal doping.

To explicitly isolate the effect of the interlayer coupling, figure 7(b) displays the evolution of $\tilde{\Delta}_{SC}$ versus $J_\perp^x/J_\parallel^x$ at several fixed fillings. Once the interlayer exchange surpasses the intralayer exchange, $J_\perp^x > J_\parallel^x$, $\tilde{\Delta}_{SC}$ exhibits a steady, monotonic increase across all evaluated filling levels. As shown in figure 7(d), the pairing configuration in this interlayer strongly-coupled regime is dominated by an interlayer s-wave pattern, rendering the intralayer pairing effectively negligible.

The emergence of the interlayer s-wave state and its associated high T_c can be intuitively understood through the concept of pairing frustration [129]. In a pure intralayer pairing scenario, a given electron must pair with one of its four in-plane neighbors, leading to spatial competition and geometric frustration. In contrast, an electron couples exclusively with the single adjacent site across the vertical rung. This absence of geometrical frustration allows the strong $J_\perp^x$ to establish a dominant, uniform vertical pairing state.

Within SBMF, the physical order parameter $\tilde{\Delta}_{SC} = \delta\Delta_{pair}$ increases with the assumed $J_\perp^x$ [129]. This trend is consistent with the concurrence of SC and a straighter inner-apical bond, and with the suppression of SC by inner-apical oxygen vacancies. In the model, straightening of the inner Ni–O–Ni bond enhances the exchange path and increases the calculated $J_\perp^x$. Inner-apical oxygen vacancies strongly weaken this path and suppress the calculated rung-pairing amplitude. These trends are consistent with the observed sensitivity of SC to the local oxygen environment.

Within the strong coupling scenario, the intrinsic carrier concentration places the itinerant $3d_{x^2-y^2}$ band deep in the overdoped regime. The nominal filling of this orbital is 0.5 electrons per site corresponding to a quarter-filled band. Relative to a half-filled Mott insulating state, this equates to an effective hole-doping concentration of $\delta = 0.5$. This value is significantly higher than the typical optimal hole-doping ~ 0.16 observed in cuprate superconductors. As a result, introducing electrons into the system (electron doping) reduces the effective hole concentration, pushing the system closer to optimal doping. The model therefore predicts an enhancement of the pairing scale under electron doping. This prediction can be tested through controlled carrier doping [129, 218].

To capture strong correlation effects beyond mean-field approximations, further efforts have employed the variational Monte Carlo (VMC) method [201]. VMC calculations for the effective model also find dominant interlayer pairing and yield a larger ground-state pairing amplitude than SBMF theory over the studied parameter range. This result suggests that interlayer pairing correlations can remain sizable at smaller $J_\perp^x$ within the effective model. This quantitative difference is crucial for real materials.

Consistent conclusions have been drawn from other studies utilizing this effective single-orbital framework. For example, [142] investigated the pairing mechanism by analyzing a t–$J_\perp$–U model, which explicitly induces the on-site Hubbard repulsion U alongside the effective spin-exchange interactions.

They found that a large U strongly suppress the kinetic energy of the itinerant electrons. Due to this correlation-induced bandwidth narrowing, the relative importance of the interlayer magnetic exchange is effectively amplified. A stable superconducting state can emerge even for smaller values of $J_{\perp}^{x}$, further reinforcing the viability of this pairing mechanism.

4.2. Strong interlayer $J_{\perp}$ limit

This strong-interlayer model provides an orbital-resolved limiting comparison. In the Hund-assisted reduction discussed above, the $3d_{z^2}$ sector supplies the gapped interlayer magnetic correlations, and the $3d_{x^2-y^2}$ carriers provide the superconducting phase coherence. To gain deeper physical insight into the mechanisms governing T_c, it is instructive to examine the asymptotic limit of extremely strong interlayer exchange ($J_{\perp} \to \infty$) [140]. In this regime, the problem simplifies into a competition between the intralayer kinetic hopping and the formation of localized interlayer spin singlets. The relevant physics is captured by an effective Hamiltonian:

$$H_{\text{eff}} = -t_{\parallel} \sum_{\langle i,j\rangle \alpha\sigma} \mathcal{P}\left(d^{\dagger}_{\alpha\sigma}(i)\, d_{\alpha\sigma}(j) + \text{h.c.}\right)\mathcal{P} + J_{\perp} \sum_{i} \boldsymbol{S}_1(i) \cdot \boldsymbol{S}_2(i). \tag{9}$$

This theoretical framework can be applied to both the $3d_{z^2}$ orbital and $3d_{x^2-y^2}$orbitals, albeit at vastly different effective doping levels.

Energetically, a dominant $J_{\perp}$ strongly favors the formation of tightly bound interlayer spin singlets, as illustrated previously in figure 6. At exact half-filling, the formation of these rung singlets results in a symmetric mass generation (SMG) insulator [140]. Unlike standard antiferromagnets, this state is a featureless Mott insulator unique to bilayer systems, arising because the strict bilayer geometry cancels the Lieb-Schultz-Mattis anomaly. In this limit, the electronic degrees of freedom are locked into local rungs and can be effectively mapped to hard-core bosons, yielding an equivalent single-layer bosonic model. SC then naturally emerges upon doping this SMG insulator. The injected carriers mobilize these preformed Cooper pairs, allowing them to establish macroscopic phase coherence.

Physically, the effective T_c in this scenario is determined by the lower of two characteristic energy scales: the pairing temperature T_{pair} dictated by interlayer superexchange, and the phase-coherence temperature T_{phase} governed by the kinetic hopping of those preformed pairs. The evolution between the strong-coupling BEC-like regime and weak-coupling BCS regime is therefore explicitly controlled by the dimensionless ratio $J_{\perp}/t_{\parallel}$ [140].

In the strong-coupling BEC limit, which applies to the nearly half-filled $3d_{z^2}$ orbitals, the pairing energy is large. Preformed rung Cooper pairs emerge at a high pairing temperature T_{pair}, but they remain initially phase-incoherent. The actual superconducting T_c is therefore entirely determined by the phase-ordering BEC temperature T_{phase}. Within a perturbative approximation, the effective kinetic hopping of these preformed pairs is given by $\tilde{t} = 8t_{\parallel}^2/3J_{\perp}$. Because T_c is directly proportional to this effective pair mobility, it decreases as the interlayer coupling $J_{\perp}$ increases. Physically, as the pairs become more tightly bound, their effective mass increases, severely hindering the establishment of macroscopic phase coherence.

Conversely, the BCS-like regime better captures the physics of the highly overdoped $3d_{x^2-y^2}$ orbitals. In this regime, local pair formation and the establishment of global phase coherence occur almost simultaneously. Here, T_c is primarily limited by the superconducting pairing gap itself, which scales positively with the magnetic interaction strength. Because the itinerant $3d_{x^2-y^2}$ band resides on the BCS side of the crossover, enhancing the interlayer exchange $J_{\perp}$ directly elevates T_c. This analytical conclusion is consistent with the numerical phase diagrams derived from the effective single-orbital models.

As summarized in table 1, the interplay between kinetic hopping and magnetic exchange results in a non-monotonic dependence of T_c on both the interaction strength and the band filling [140]. Theoretically, the maximum of T_c is achieved within the intermediate BCS-BEC crossover region, where the pairing strength and the phase-coherence scales are optimally balanced. Regarding the electron filling, T_c peaks near a quarter-filled configuration ($x = 1/4$). At this specific filling, the interlayer Cooper pairs acquire sufficient kinetic mobility while maintaining a robust pairing amplitude.

This physical picture establishes a dichotomy between the two active Ni $3d$ orbitals [140]. Because the highly itinerant $3d_{x^2-y^2}$ electrons reside on the weak-coupling BCS side of the crossover, the T_c of this sector is expected to increase upon electron doping. Adding electrons reduces the effective hole concentration (δ), pushing the system toward the optimal crossover regime. In contrast, the nearly half-filled $3d_{z^2}$ band sits deep within the strong-coupling BEC limit. For this orbital, T_c would be enhanced by hole doping, which introduces the mobile carriers necessary for the otherwise localized rung pairs to establish macroscopic phase coherence. The opposite doping trends predicted for the two limits provide a possible experimental discriminator when combined with orbital-resolved measurements.

Table 1. Parameter estimation and theoretically predicted T_c for the Ni $3d_{x^2-y^2}$ and $3d_{z^2}$ electrons. Here, x denotes the electron filling fraction, $t_{\parallel}$ is the intralayer hopping amplitude, $J_{\perp}$ is the interlayer AFM superexchange, and T_c is the estimated superconducting transition temperature. Reproduced from [140]. CC BY 4.0.

Parameters	$3d_{x^2-y^2}$ electron	$3d_{z^2}$ electron
x	$1/4$	$1/2 \rightarrow 0.483$
$t_{\parallel}$	0.48 eV	~ 0.1 eV
$J_{\perp}$	~ 0.66 eV	~ 0.66 eV
$J_{\perp}/t_{\parallel}$	1.4	6.6
$T_c/t_{\parallel}$	0.014	$0 \rightarrow 0.067$
T_c	79 K	$0 \rightarrow 78$ K
SC order	s-wave interlayer spin-singlet	
Mechanism	BCS	BEC

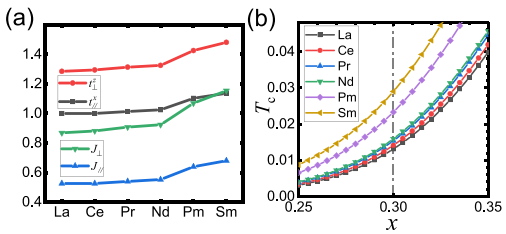


Figure 8. (a). Calculation of the relevant hopping integrals and effective spin-exchange parameters for the isostructural $R_3Ni_2O_7$ (R = La, Pr, Nd, Sm) in the high-pressure Fmmm phase. As the rare-earth element changes from La to Sm, both the interlayer $3d_{z^2}$ hopping $t_{\perp}^z$ and intralayer $3d_{x^2-y^2}$ hopping $t_{\parallel}^x$ gradually increase [136]. The corresponding magnetic exchange parameters $J_{\perp}$ and $J_{\parallel}$ follow a similar monotonic trend. (b). SBMF calculated transition temperature as a function of the $3d_{x^2-y^2}$ filling x in the effective model. At fixed x, the calculated T_c increases from La to Sm; the filling relevant to $La_3Ni_2O_7$ is estimated to be near $x \simeq 0.3$. Reproduced from [143]. © IOP Publishing Ltd. All rights reserved.

4.3. Element substitution

The discovery of SC near 80 K in pressurized $La_3Ni_2O_7$ has motivated efforts to further elevate T_c via chemical tuning. A standard approach is rare-earth element substitution, synthesizing the isostructural $R_3Ni_2O_7$ series (where R = La to Sm). Within the high-pressure *Fmmm* phase, replacing La with smaller rare-earth ions acts as effective chemical pressure, systematically reducing the lattice constants [136]. The Ni atoms are brought closer together, directly enhancing the spatial overlap of the adjacent Ni $3d$ wavefunctions.

Driven by the enhanced overlap, both the intralayer hopping $t_{\parallel}^x$ of the $3d_{x^2-y^2}$ orbitals and the interlayer hopping $t_{\perp}^z$ of the $3d_{z^2}$ orbitals increase monotonically from La to Sm. First principle calculations predict such variation under element substitution, as depicted in figure 8(a) [136]. Since the relevant magnetic superexchange interactions scale approximately as $J_{\perp} \sim (t_{\perp}^z)^2/U$ and $J_{\parallel} \sim (t_{\parallel}^x)^2/U$, they are considerably amplified by this structural compaction.

Strong-coupling SBMF calculations based on these material parameters find that the interlayer *s*-wave state remains dominant across the rare-earth series [143]. At a fixed $3d_{x^2-y^2}$ filling, the calculated pairing amplitude and T_c increase from La to Sm, as shown in figure 8(b). Within the strong coupling picture, the increase of $t_{\perp}^z$ strengthens the interlayer exchange in the $3d_{z^2}$ sector. Hund's coupling further transfers this enhanced interlayer magnetic correlation to the effective interlayer interaction between the itinerant $3d_{x^2-y^2}$ carriers. This predicts a enhancement of T_c for the structural trend across the rare-earth series [143, 218].

Recent high-pressure experiments have reported bulk SC with an onset T_c up to 96 K in partially Sm-substituted $La_{3-x}Sm_xNi_2O_{7-\delta}$ crystals [32]. Nd-substituted $La_{3-x}Nd_xNi_2O_7$ samples have also shown a resistive onset near 93 K and a radio-frequency signature near 100 K [31]. These experimental results demonstrate that partial rare-earth substitution can raise the superconducting transition scale. The observed trend follows the direction of the strong-coupling prediction. The calculations treat fully substituted compounds in the *Fmmm* structure, whereas the experiments concern partially substituted samples with their own pressure-induced structural evolution.

Weak-coupling theory for the substituted series predicts a decreasing pairing scale with decreasing rare-earth ionic radius [136]. The origin of the different theoretical trends is discussed in section 6.

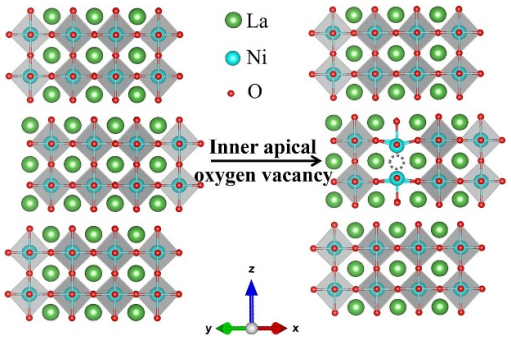


Figure 9. Structural comparison between pristine $La_3Ni_2O_7$ and the oxygen-deficient $La_3Ni_2O_{7-\delta}$, projected along the [110] axis. The left panel displays the ideal lattice structure of $La_3Ni_2O_7$ composed of alternating NiO_2 and LaO layers. The right panel illustrates the defective structure with a missing apical oxygen, indicated by a black dashed circle. Reproduced from [192]. CC BY 4.0.

4.4. Effect of pressure and apical oxygen vacancies

The emergence of high-T_c SC in $La_3Ni_2O_7$ is highly sensitive to its structural geometry and oxygen stoichiometry. To capture these material-specific details, studies have investigated the impact of external pressure and apical oxygen vacancies by simulating the effective bilayer t–$J_{\parallel}$–$J_{\perp}$ model within a real-space SBMF framework [192]. The pressure-dependent hopping parameters give an enhanced effective $J_{\perp}^{x}$ in the high-pressure phase. At a fixed filling $x = 0.25$, the calculated T_c increases from approximately 15 K at ambient pressure to nearly 87 K at 30 GPa [192]. This enhancement is qualitatively consistent with the emergence of high-T_c SC under pressure.

Experimental phase diagrams reveal a non-monotonic trend under pressure, where T_c eventually decreases once the pressure exceeds an optimal value. Within the strong-coupling calculation, this high-pressure suppression is associated with the ratio $J_{\perp}^{x}/J_{\parallel}^{x}$. DFT calculations indicate that the hopping ratio $t_{\perp}^{z}/t_{\parallel}^{x}$ decreases under further compression [130]. In the parameterization of the effective model, this produces a corresponding decrease in $J_{\perp}^{x}/J_{\parallel}^{x}$. SBMF calculations find that T_c decreases rapidly as this ratio is reduced [192]. The increasing intralayer pairing tendency then competes with the interlayer s-wave channel and lowers the calculated T_c.

Inner-apical oxygen vacancies locally interrupt the bilayer rung and strongly suppress SC in the real-space calculation. As shown in figure 9, an apical vacancy is the absence of the central oxygen atom connecting the upper and lower NiO_2 planes within a bilayer rung. At this specific defect site, the vertical hopping $t_{\perp}^{z}$ between the $3d_{z^2}$ orbital essentially vanishes because the mediating oxygen $2p_z$ orbital is missing. In the reduced $3d_{x^2-y^2}$ model, this effect is represented by setting the corresponding effective exchange $J_{\perp}^{x}$ to zero. Since $J_{\perp}^{x}$ controls the dominant interlayer pairing channel in this model, a finite vacancy concentration suppresses both local rung pairing and the global superconducting response.

Real-space numerical simulations of random apical oxygen vacancies find that the spatially averaged interlayer pairing amplitude decreases with increasing vacancy concentration [192]. The broken hopping path also modifies the local charge distribution and reduces the calculated low-energy density of states (DOS) around the defect. In these calculations, the vacancies behave as strong pair-breaking defects that suppress both the local rung-pairing amplitude and the global superfluid density [192]. The spatial disorder introduced by random vacancies suppresses the macroscopic diamagnetic current while simultaneously enhancing the opposing paramagnetic current. The resulting reduction of the superfluid response may be relevant to the weak diamagnetic signal and filamentary superconducting behavior reported in oxygen-deficient samples [44].

4.5. Theoretical proposal for electric-field tuning in thin films

The pairing properties of the bilayer models depend crucially on both the effective magnetic coupling and the orbital filling levels. Under intrinsic conditions, the bilayer structure is symmetric, maintaining equal carrier concentration across the two NiO_2 layers. The realization of superconducting bilayer nickelate films provides a platform for electrically tuning these correlated states. A perpendicular electric field introduced through electrostatic gating offers a possible means of creating a layer-dependent carrier density [211].

A perpendicular electric field breaks the spatial inversion symmetry of the bilayer, driving a redistribution of electrons from the higher-potential layer to the lower-potential one, as depicted in figure 10. In the two-orbital calculation, this charge redistribution is strongly orbital selective. The nearly half-filled

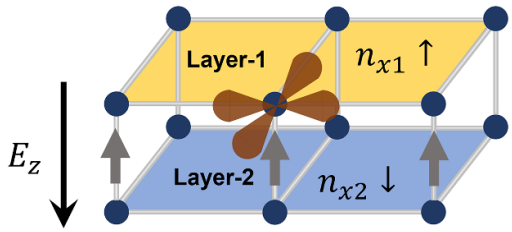


Figure 10. Schematic of the electron redistribution induced by a perpendicular electric field, E_z. Driven by the external field, electrons migrate toward the lower-potential layer. This interlayer charge transfer selectively modifies the filling of the itinerant $3d_{x^2-y^2}$ orbitals, resulting in a higher electron density n_{x1} in layer 1 compared to n_{x2} in layer 2.

$3d_{z^2}$ sector has a comparatively rigid occupancy under the local crystal field splitting and Hubbard interaction. The transferred charge therefore enters predominantly the more itinerant $3d_{x^2-y^2}$ orbitals in the lower-potential layer [211]. This orbital-selective mechanism effectively electron-dopes one layer while hole-doping the other, modifying the intralayer physics without chemical substitution.

This electric-field-driven orbital-selective filling alters the pairing picture. The resulting layer imbalance shifts the relative Fermi levels of the two $3d_{x^2-y^2}$ bands and produces a Fermi-surface mismatch. In the effective model, this mismatch acts as a pseudo-Zeeman field on the layer index and suppresses interlayer spin-singlet pairing.

As the interlayer *s*-wave pairing is weakened, the charge-accumulated layer approaches a filling regime favorable for intralayer *d*-wave pairing. A robust intralayer *d*-wave superconducting pairing emerges within this specific layer. The SBMF solution develops a predominantly intralayer *d*-wave state in this layer, while DMRG calculations find enhanced intralayer *d*-wave pairing correlations under the layer imbalance [211]. For the parameters adopted in the calculation, SBMF predicts that an interlayer potential difference of approximately 0.1–0.2 V can raise the mean-field T_c above 77 K. The relation between this interlayer potential difference and an externally applied gate voltage depends on screening and device geometry.

The two-orbital SBMF calculation further finds a mixed-symmetry solution [211]. The $3d_{z^2}$ sector retains interlayer *s*-wave pseudogap correlations, while the itinerant $3d_{x^2-y^2}$ orbitals in the charge-accumulated layer support intralayer *d*-wave SC. At the mean-field level, the two components acquire a relative phase of $\pi/2$, producing a $d+is$ solution that breaks time-reversal symmetry.

Electrostatic gating therefore provides a way to tune the layer fillings without intentionally introducing substitutional disorder. These predictions motivate gate-tuning experiments on superconducting bilayer films and suggest a possible route for controlling the competition between interlayer and intralayer pairing.

4.6. Strong-coupling interpretation of T_c-tuning trends

Recent theoretical work [218] proposes the effective interlayer exchange $J_\perp$ and the $3d_{x^2-y^2}$ filling as two organizing parameters for several T_c-tuning trends in bilayer nickelates. The calculated evolution under pressure, epitaxial strain, and element substitution is qualitatively consistent with the corresponding experimental trends [25, 31, 32, 35, 37]. Structural tuning changes several microscopic parameters simultaneously, and their relative contributions to T_c remain open.

In the DFT-derived parameter sets used in this calculation, compressive epitaxial strain and the reduced *c*-axis lattice constant associated with rare-earth substitution enhance the $3d_{z^2}$ interlayer hopping and exchange $J_\perp^z$. The corresponding effective $J_\perp$ in the reduced $3d_{x^2-y^2}$ model increases and produces a higher calculated T_c. Under continuous external pressure, the DFT-derived $J_\perp^z$ shows a nonmonotonic evolution associated with the straightening of the inner-apical bond at lower pressures and the pressure-induced shift of the O-p_z level at higher pressures [174, 187]. The mapped effective $J_\perp$ and the calculated T_c follow a similar nonmonotonic trend, qualitatively consistent with the observed pressure dependence [35].

Beyond isovalent structural tuning, this framework has also been applied to chemical doping [218]. Within the model, hole doping reduces the $3d_{x^2-y^2}$ filling, moves the system farther into the overdoped side of the calculated phase diagram, and suppresses the pairing amplitude. This trend is qualitatively consistent with the reported suppression of SC in hole-doped samples [28, 33, 67, 103]. The experimental tuning can also modify the local structure, leaving the quantitative contribution of carrier filling open.

The calculated phase diagram is particle-hole asymmetric and predicts an enhancement of pairing under electron doping. Introducing electron doping, potentially through higher-valence elements, would increase the $3d_{x^2-y^2}$ filling and push the system closer to the optimal pairing strength. Controlled electron doping is therefore proposed as a possible route to higher T_c and provides a direct experimental test of the calculated doping asymmetry.

5. Interplay between the two orbitals

The effective single-orbital model isolates interlayer pairing of the $3d_{x^2-y^2}$ carriers. A two-orbital treatment is needed to describe the redistribution of charge between the two E_g orbitals and its evolution under doping. This is particularly crucial for understanding the system's global phase diagram and its response to chemical doping. In this situation, it is instructive to define the total hole-doping level, $\delta_{\rm tot}$, relative to the $3d^8$ configuration (Ni^{2+}) where each E_g orbital is half-filled. For pristine $La_3Ni_2O_7$, the nominal Ni valence is +2.5 ($3d^{7.5}$), which corresponds to a doped state with $\delta_{\rm tot} = 0.5$. Consequently, introducing additional electrons into the pristine material equates to reducing the total hole concentration to $\delta_{\rm tot} < 0.5$.

To explicitly capture this interorbital physics and the Hund-assisted pairing mechanism, a strong-coupling bilayer two-orbital *t–J* model is formulated [167]. Within this framework, the distinct spatial characteristics of the two orbitals dictate their specific roles. The relatively localized $3d_{z^2}$ orbitals establish a direct and robust interlayer AFM superexchange. Meanwhile, the itinerant $3d_{x^2-y^2}$ electrons experience two distinct magnetic interactions, the intralayer AFM exchange within the NiO_2 planes, and the effective interlayer AFM coupling transmitted from the $3d_{z^2}$ spins via the on-site Hund's rule.

These magnetic interactions are formally described by the exchange Hamiltonian H_J:

$$H_J = J_{\parallel}^{x} \sum_{\langle i,j\rangle\alpha} \boldsymbol{S}_{x\alpha}(i)\cdot\boldsymbol{S}_{x\alpha}(j) + J_{\perp}^{x}\sum_{i}\boldsymbol{S}_{x1}(i)\cdot\boldsymbol{S}_{x2}(i) + J_{\perp}^{z}\sum_{i}\boldsymbol{S}_{z1}(i)\cdot\boldsymbol{S}_{z2}(i), \tag{10}$$

Since the $3d_{z^2}$ orbital remains strongly correlated and nearly localized, the effective Hund-assisted pairing strength approximately equals the bare interlayer exchange $J_{\perp}^{x} \approx J_{\perp}^{z}$ in the extreme Hund's coupling limit ($J_{\rm H} \to \infty$). The total Hamiltonian is given by $H = H_0 + H_J$. Here, the kinetic part H_0 is identical to the tight-binding Hamiltonian previously defined in equation (1), which intrinsically incorporates the interorbital and inter-site hybridizations.

This strongly correlated model can be solved using the SBMF theory, where auxiliary slave particles (charged holons and neutral spinons) are introduced independently for each orbital [167]. To simplify the analysis and isolate the dominant pairing mechanism, the mean-field decoupling of these AFM exchange interactions is restricted to the relevant interlayer pairing channels. For a given $\delta_{\rm tot}$, the holon density of each orbital is determined self-consistently upon simulation.

5.1. Orbital-selective band renormalization

Within the two-orbital SBMF treatment based on the high-pressure band structure, correlations produce an orbital-dependent band renormalization. The stronger calculated renormalization of the $3d_{z^2}$ states is qualitatively consistent with the orbital differentiation observed by ARPES in ambient-pressure bulk samples [40]. Direct orbital-resolved measurements of the superconducting high-pressure phase are not yet available. Within the strong-coupling limit, the coherent propagation of electrons is strictly governed by the no-double-occupancy constraint. In the SBMF formulation, this physical restriction dictates that the effective kinetic hopping of the spinons is directly modulated by the local holon density, an electron can only hop to an available empty site. As an orbital approaches half-filling where the holon density vanishes, its effective spinon hopping amplitude is severely suppressed, leading to a flattened band.

Since the $3d_{z^2}$ orbital is nearly half-filled, its holon density is exceptionally small, subjecting it to intense correlation effects. This $3d_{z^2}$ band is pushed toward a Mott-like localized state, resulting in a significantly reduced quasiparticle weight and a large enhancement of its effective mass. Conversely, the nearly quarter-filled $3d_{x^2-y^2}$ orbital possesses a larger holon density and thus experiences a weaker mass enhancement. These $3d_{x^2-y^2}$ electrons retain a largely itinerant character and dominate the macroscopic charge transport. This stark orbital differentiation is captured by the SBMF numerical calculations, as illustrated by the contrast between the non-interacting and strongly correlated band structures in figure 11 [167]. This theoretical picture provides a possible strong-coupling account of the orbital-dependent band renormalization observed by ARPES [40].

This orbital differentiation provides the physical basis for the pairing mechanism. The heavily renormalized $3d_{z^2}$ electrons establish the strong interlayer AFM superexchange, effectively acting as a robust

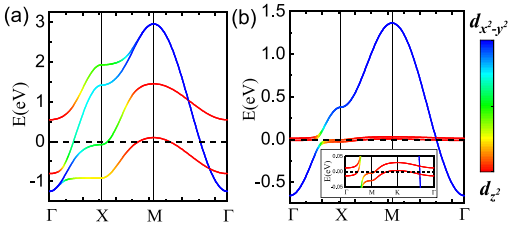


Figure 11. (a) Non-interacting tight-binding band structure (originally from [141] shown for comparison). (b) Strongly correlated spinon band structure derived from SBMF theory. The color scale indicates the orbital character, with red and blue representing the $3d_{z^2}$ and $3d_{x^2-y^2}$ orbitals, respectively. The system features four bands corresponding to the two active orbitals and their bonding/antibonding combinations. In the strong-coupling Mott limit, electronic correlations flatten the $3d_{z^2}$-dominated bands and reduce the bonding-antibonding splitting. High-symmetry momentum points in the Brillouin zone are marked as $\Gamma(0,0)$, $X=(\pi,0)$, $M=(\pi,\pi)$. The inset in (b) provides a zoomed-in view of the highly renormalized dispersion near the Fermi level. Reprinted (figure) with permission from [167], Copyright (2024) by the American Physical Society.

stationary background. The relatively light $3d_{x^2-y^2}$ electrons interact with these localized spins via the on-site Hund's rule coupling. This clear division of labor allows the itinerant carriers to dynamically acquire pairing interactions from the $3d_{z^2}$ sector while maintaining the kinetic energy required for macroscopic phase coherence. Within the strong-coupling model, this orbital differentiation motivates an orbital-dependent description of pairing.

5.2. Orbital-dependent pseudogap and global phase diagram

The global phase diagram of bilayer nickelates is shaped by the interplay between the two active orbitals. Within the SBMF framework [5, 167, 242], the onset of SC and the emergence of a pseudogap phase are governed by two characteristic temperature scales, the spinon pairing temperature T_{pair} and the holon condensation temperature T_{phase}. For either orbital sector, because establishing a coherent superconducting state requires both local pair formation and macroscopic phase coherence, the orbital-specific transition temperature is determined by $\min(T_{\text{pair}}, T_{\text{phase}})$. These orbital-resolved scales organize the calculated SBMF phase diagram and identify which sector limits the single global superconducting transition.

For the nearly half-filled $3d_{z^2}$ orbital, the strong interlayer AFM exchange favors the formation of vertical rung singlets at a high pairing temperature, T^z_{pair}. However, because these localized electrons possess a large effective mass, the preformed pairs lack the kinetic mobility necessary to establish long-range phase coherence. Their phase-ordering temperature T^z_{phase} is significantly lower than T^z_{pair}. This places the $3d_{z^2}$ orbital deep in the strong-coupling BEC-like regime, where its actual superconducting transition is controlled by phase coherence, yielding $T^z_c = T^z_{\text{phase}}$.

In the wide temperature window between T^z_{phase} and T^z_{pair}, the $3d_{z^2}$ orbital remains non-superconducting. In the SBMF solution, the presence of preformed local pairs manifests as an interlayer *s*-wave pseudogap, characterized by a distinct suppression of the electronic DOS well above T^z_c. Crucially, because the intrinsic $3d_{z^2}$ band resides in the heavily underdoped regime close to half-filling, introducing hole doping systematically increases its holon density. This injection of mobile carriers enhances the kinetic mobility of the system, thereby raising the phase-coherence temperature T^z_{phase} and pushing the localized sector $3d_{z^2}$ toward a coherent superconducting state.

In contrast to the localized $3d_{z^2}$ states, the itinerant $3d_{x^2-y^2}$ electrons dynamically acquire an effective interlayer pairing interaction via the on-site Hund's coupling Because these electrons are highly mobile, their intrinsic phase-coherence scale T^x_{phase} is inherently large, remaining well above their characteristic pairing temperature T^x_{pair}. Therefore, within this orbital sector, local pair formation and global phase coherence occur almost simultaneously. This places the $3d_{x^2-y^2}$ band in the BCS-like regime, where its actual superconducting transition is directly determined by the pairing strength itself, yielding $T^x_c \approx T^x_{\text{pair}}$.

The doping response of this BCS-like $3d_{x^2-y^2}$ orbital is opposite to that of the BEC-like $3d_{z^2}$ orbital. Because the $3d_{x^2-y^2}$ electrons already reside in a heavily overdoped regime, further hole doping monotonically suppresses its effective pairing scale T^x_{pair}, thereby reducing T^x_c. Starting from the nominal composition of $La_3Ni_2O_7$, which corresponds to an effective total hole doping of $\delta_{\text{tot}} = 0.5$, further electron doping reduces the hole concentration. This pushes the $3d_{x^2-y^2}$ sector toward the optimal pairing regime, systematically increasing its T^x_c.

As summarized in the calculated global phase diagram figure 12 [167], the macroscopic superconducting transition of the entire bilayer system is dictated by the orbital sector exhibiting the higher critical temperature, yielding $T_c = \max(T^x_c, T^z_c)$. In the calculated phase diagram, $T^* = T^z_{\text{pair}}$ marks the onset of $3d_{z^2}$ orbital spinon pairing and defines an orbital-selective pseudogap regime within SBMF theory.

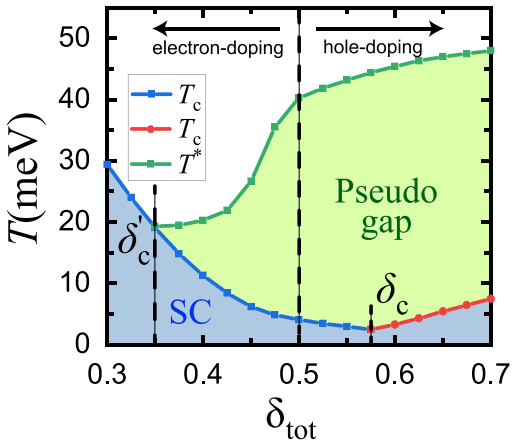


Figure 12. Theoretical phase diagram depicting the superconducting critical temperature T_c and pseudogap temperature T^* versus the total hole-doping level δ_{tot}. The nominal stoichiometry of $La_3Ni_2O_7$ corresponds to $\delta_{tot} = 0.5$. Values of $\delta_{tot} > 0.5$ and $\delta_{tot} < 0.5$ indicate physical hole and electron doping, respectively. The upper curve (T^*) marks the onset of spinon pairing in the $3d_{z^2}$ orbital, which merges into the macroscopic superconducting phase at a critical doping level δ_c'. The lower curve denotes the macroscopic superconducting T_c of the entire system, which exhibits a local minimum at δ_c. Reprinted (figure) with permission from [167], Copyright (2024) by the American Physical Society.

This extended pseudogap regime is pronounced near the intrinsic stoichiometry ($\delta_{tot} = 0.5$) and further expands under hole doping.

Near the intrinsic composition and extending deep into the electron-doped regime, the actual superconducting transition is driven by the highly itinerant $3d_{x^2-y^2}$ band ($T_c = T_c^x > T_c^z$). Because electron doping pushes this specific orbital closer to its optimal pairing strength, the macroscopic T_c of the system rises systematically with increasing electron concentration. Furthermore, in the heavily electron-doped regime ($\delta_{tot} < \delta_c'$), the $3d_{z^2}$ pairing temperature T^z_{pair} is suppressed below the macroscopic T_c. Consequently, the pseudogap phase vanishes completely, and the system transitions directly from a normal metal into the superconducting state, governed by the single $3d_{x^2-y^2}$ orbital.

As hole doping increases, the system undergoes an orbital crossover, transitioning from BCS-like to BEC-like SC [167]. Hole doping simultaneously suppresses the $3d_{x^2-y^2}$ pairing strength and enhances the $3d_{z^2}$ phase coherence. Thus, T^x_{pair} decreases while T^z_{phase} increases under hole doping. There exists a critical doping level δ_c where these two energy scales intersect. For $\delta_{tot} > \delta_c$, T^x_{pair} drops below T^z_{phase}, meaning the $3d_{z^2}$ orbital dominates the macroscopic transition, $T_c = T_c^z > T_c^x$. In this heavily hole-doped regime, T_c increases with further hole doping due to the enhanced kinetic mobility of the $3d_{z^2}$ holons. Ultimately, this orbital crossover produces a distinct non-monotonic phase boundary, where the superconducting states on either side of the minimum at δ_c are governed by entirely different active orbitals. The distinct thermodynamic and transport signatures of these two regimes (weak-coupling BCS vs strong-coupling BEC) provide possible experimental signatures for distinguishing the two calculated regimes [140, 167].

The proposed orbital-selective phase diagram highlights a distinction between bilayer nickelates and high-T_c cuprates. In cuprates, both the pseudogap and SC involve the same low-energy Cu $3d_{x^2-y^2}$ band (or its relevant Zhang-Rice singlet band). The microscopic origin of the cuprate pseudogap remains under debate. The present Hund's assisted scenario for bilayer nickelates assigns the two temperature scales mainly to different orbital sectors. Within this description, the nearly localized $3d_{z^2}$ sector hosts the calculated pseudogap scale, while Hund coupling generates an effective interlayer interaction for the itinerant $3d_{x^2-y^2}$ carriers that develop global phase coherence. Ambient-pressure ARPES has reported pseudogap-like suppression in the $3d_{x^2-y^2}$-derived spectral weight [55]. Its relation to the $3d_{z^2}$ spinon-pairing pseudogap in the SBMF phase diagram remains open. Orbital-resolved measurements in superconducting samples are needed to test this theoretical assignment [231].

5.3. Hund-assisted pairing and multi-orbital interplay

A more microscopic treatment keeps the interorbital interactions explicit. DMRG and tensor-network studies have investigated multiorbital ladder and related models containing the intra-atomic Hund interaction [150, 157, 160]. In these microscopic models, the Hund's coupling is introduced as an independent term, $H_{Hund} = -J_H \sum_i \boldsymbol{S}_{x,i} \cdot \boldsymbol{S}_{z,i}$. Retaining this explicit J_H term reveals that the macroscopic

superconducting state is not an instability of an isolated band, but a cooperative phenomenon orchestrated by multi-orbital interplay.

As anticipated, the strong vertical hybridization generates robust interlayer AFM superexchange between the nearly localized $3d_{z^2}$ orbitals. Simulations on two-orbital ladder models demonstrate that the induced singlet pairing correlations in both the $3d_{z^2}$ and the itinerant $3d_{x^2-y^2}$ bands exhibit a slow power-law (algebraic) decay, whereas the corresponding spin correlations decay exponentially [150, 157, 160]. This behavior supports the emergence of quasi-long-range superconducting correlations in the quasi-one-dimensional limit.

Importantly, these numerical results highlight the roles of two distinct yet collaborative quantum bridges, the interorbital hybridization and Hund's coupling. On the one hand, the interorbital hopping (e.g. $t_{\parallel}^{xz}$) allows the $3d_{x^2-y^2}$ band to acquire pairing signatures directly from the $3d_{z^2}$ sector via kinetic mixing [150]. In fact, DMRG calculations show that pair correlations can develop as a hybridized two-orbital entity even when Hund's coupling is artificially turned off [160]. On the other hand, the local J_{H} strongly enhances these correlations by ferromagnetically aligning the spins of the two orbitals on the same site, dynamically imprinting the spin-singlet correlations onto the $3d_{x^2-y^2}$ band. For the parameter set adopted to represent pressurized $La_3Ni_2O_7$, tensor-network calculations place the model in a Hund's-rule-dominated superconducting regime, where J_{H} provides the leading enhancement of the pairing correlations [157].

The same calculations find a nonmonotonic dependence of pairing correlations on the interorbital hybridization. Moderate hybridization cooperates with J_{H} in transferring pairing correlations between the two orbitals. Larger hybridization introduces interorbital frustration and suppresses the calculated pairing correlations [157]. The relative importance of hybridization and Hund's coupling in superconducting bilayer nickelates remains to be determined. The suppression at large hybridization may be relevant to the decrease of T_c at higher pressures [35].

5.4. Mixed Spin-1 and Spin-1/2 Pairing Mechanism in Bilayer Nickelates

An alternative theoretical perspective approaches bilayer nickelates from the extreme strong-coupling limit, treating the Hubbard repulsion U and the on-site Hund's coupling J_{H} as the dominant energy scales [194]. In this regime, the strong ferromagnetic J_{H} tightly binds the electrons in the two active E_{g} orbitals, causing each Ni^{2+} ion (nominal $3d^8$ configuration) to act as an effective, localized spin-1 magnetic moment. Upon hole doping towards the physical $Ni^{2.5+}$ state ($3d^{7.5}$) of bilayer nickelate, electrons are preferentially removed from the itinerant $3d_{x^2-y^2}$ orbitals. This process converts a fraction of the local spin-1 triplets into spin-1/2 moments, which primarily reside in the remaining $3d_{z^2}$ orbitals. This interplay between superexchange and Hund's coupling, and the resulting competition among various spin states, has also been extensively discussed within the context of Type-II t–J models [131, 146, 169, 206, 207, 212, 213].

Building upon this strong-coupling, local-moment picture, a detailed mechanism for SC has been developed by focusing on the actual doping process, where a mixed spin-1 and spin-1/2 bilayer t–J model has been proposed and simulated [194]. This framework treats the nominal $3d^8$ configuration ($\delta_{\mathrm{tot}} = 0$) as the underlying Mott insulating parent state. In this undoped limit, the strong interlayer hybridization of the $3d_{z^2}$ orbitals generates an AFM superexchange that magnetically locks the local spin-1 moments into spin-1 interlayer rung singlets, as depicted in the left panel of figure 13. The parent state thus behaves as a spin-1 valence bond solid (VBS) and SC emerges from doping this VBS into a mixed-spin manifold.

Upon hole doping, the strong vertical hybridization similarly drives the newly emerged $3d_{z^2}$ spin-1/2 moments to form vertical spin-1/2 singlets, as depicted in the right panel of figure 13. This local pairing minimizes the exchange energy along the c-axis. Conversely, a mixed spin-1/spin-1/2 rung suffers an energy penalty and is effectively suppressed [194]. The doped system thus consists mainly of a mixture of spin-1 and spin-1/2 rung singlets.

To achieve macroscopic phase coherence, these localized singlets must acquire kinetic mobility. Here, the two active orbitals play distinct but highly cooperative roles. In this calculation, the more localized $3d_{z^2}$ sector contributes mainly through local rung correlations, while the larger coherent pairing amplitude resides in the $3d_{x^2-y^2}$ sector. When a $3d_{x^2-y^2}$ hole hops to an adjacent site within the NiO_2 plane, it triggers a dynamic interconversion. A neighboring spin-1 rung singlet is converted into a spin-1/2 rung singlet, and vice versa [194]. This continuous intralayer charge transfer enables the vertical pairs to interconvert and propagate coherently across the two-dimensional lattice, eventually condensing into a macroscopic superconducting state.

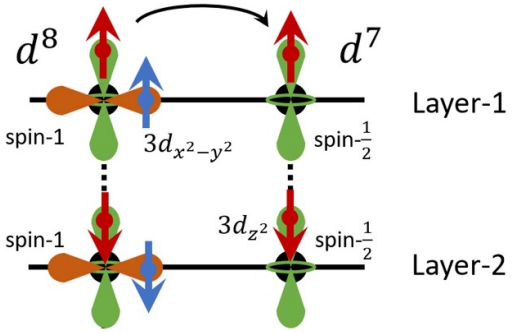


Figure 13. Schematic illustration of the two distinct types of interlayer singlet bonds on a vertical bilayer rung. The left panel shows a singlet bond formed between two local spin-1 triplets, characteristic of the undoped $3d^8$ parent state. The right panel displays a singlet bond formed between two local $3d^7$ spin-1/2 moments (predominantly $3d_{z^2}$ electrons), which emerges as the system is hole-doped toward the physical $3d^{7.5}$ configuration. Reprinted (figure) with permission from [194], Copyright (2025) by the American Physical Society.

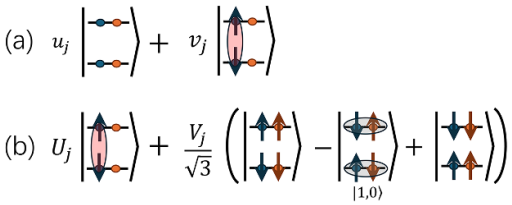


Figure 14. Schematic diagrams comparing (a) conventional BCS pairing and (b) the strongly correlated mixed-spin pairing. The conventional BCS state is represented as a coherent superposition of a paired electron state and the vacuum state. The correlated pairing state involves a coherent superposition of two distinct valence bond singlets, one formed by local spin-1 triplets and the other by local spin-1/2 moments. Blue and orange circles represent the $3d_{z^2}$ and $3d_{x^2-y^2}$ orbitals, respectively. The notation $|1,0\rangle$ indicates a local triplet state with a total spin $S = 1$ and projection $S^z = 0$. Reprinted (figure) with permission from [194], Copyright (2025) by the American Physical Society.

Consequently, the underlying pairing structure differs from the conventional BCS construction. As schematically shown in figure 14(a), a conventional BCS wavefunction is formulated as a coherent superposition of a paired-electron state and an empty vacuum state. In the present strong-coupling two-orbital scenario, however, the superconducting condensate is characterized by a coherent quantum superposition of two distinct valence bonds. As illustrated in figure 14(b), the ground state is a superposition of the spin-1/2 rung singlets (formed by the localized $3d_{z^2}$ moments) and the spin-1 rung singlets (formed by the localized triplets). Within the mixed-spin model, SC arises from coherent fluctuations between the spin-1 and spin-1/2 rung-singlet configurations.

SBMF and DMRG calculations for this model find dominant spin-singlet interlayer pairing in the $3d_{x^2-y^2}$ channel, with a smaller coherent contribution from the more localized $3d_{z^2}$ sector [194]. To bridge the gap between the abstract mixed-spin manifold and experimental observables, the superconducting state is projected back onto the physical electron basis to extract orbital-specific pairing amplitudes. These calculations consistently demonstrate that the itinerant $3d_{x^2-y^2}$ electrons constitute the dominant superconducting channel. In contrast, the $3d_{z^2}$ orbital contributes minimally to the coherent condensate due to its inherent localization. Notably, all triplet pairing channels are found to be exponentially suppressed, leaving a spin-singlet interlayer state in the calculations.

Furthermore, the macroscopic pairing amplitude exhibits a marked asymmetry with respect to doping [194]. Consistent with the previously discussed *t–J* models, electron doping is found to strengthen the superconducting order, whereas hole doping is detrimental. Mechanistically, electron doping drives the system closer to the $3d^8$ configuration, thereby increasing the local occupancy of spin-1 triplets. This enrichment of the spin-1 component enhances the formation of the corresponding rung singlets, providing a more robust magnetic background for the itinerant carriers. The mixed-spin calculation also predicts an enhancement of the superconducting order under electron doping, consistent with the trend obtained from the effective *t–J* models.

Table 2. Comparison of representative pairing approaches for bilayer nickelates. Similar gap symmetries may arise from distinct microscopic mechanisms.

Proposed mechanism	Low-energy degrees of freedom	Role of $3d_{z^2}$ and γ-pocket	Pairing states	Key tests
Hund's-rule physics assisted pairing [129, 157, 167, 194, 218, 231]	Localized $3d_{z^2}$ moments; itinerant $3d_{x^2-y^2}$ carriers; onsite J_H	Effective interlayer AFM exchange; γ-pocket not required	Interlayer s wave; possible $s+id$ near competing s/d regime	Bonding-antibonding sign change; orbital-selective diagonal gaps; electron-doping trend
Itinerant spin-fluctuation [118, 119, 128, 161]	Multiorbital Fermi surfaces	Active coherent γ pocket; interband scattering	Extended-s ($s_\pm$); d_{xy}; $d_{x^2-y^2}$	γ-band Lifshitz transition; even/odd spin resonances; U/W dependence
Cuprate-like intralayer pairing [171]	Hybridized Ni $3d_{x^2-y^2}$-O $2p$ states; intralayer AFM exchange	Self-doping reservoir; not the primary pairing channel	Most likely d wave; possible $d+is$	Intralayer magnetic response; $3d_{x^2-y^2}$ filling dependence; charge-transfer signatures
Self-doping molecular Mott insulator [135, 196, 222, 226]	Correlated bonding and antibonding molecular orbitals; molecular-Mott regime	Molecular-like interlayer bonding orbital	d wave; extended-s	Molecular-orbital character; hole-doping and orbital-filling dependence
Hybridization-assisted pairing [126, 134, 138, 200]	Local $3d_{z^2}$ rung singlets; itinerant $3d_{x^2-y^2}$ band; interorbital hybridization	Local rung correlations; hybridization-enabled coherence	Multiband extended-$s_\pm$	Nonmonotonic gap function dependence on hybridization
Multiorbital pairings based on DMFT [139, 156, 173, 189]	Dynamical two-E_g description; Hund coupling; interorbital hopping	Incoherent-to-coherent crossover; interorbital spin transfer	$s_\pm$ pairing	Quasiparticle weights; local spin response; orbital-resolved gaps

6. Comparison of theoretical approaches

Current experiments remain compatible with several coupling regimes. The theoretical literature on superconducting pairing in bilayer nickelates continues to expand rapidly, and the discussion here covers several representative approaches. Weak-to-intermediate-coupling theories and local strong-coupling models can be viewed as different limits of the multiorbital Hamiltonian. The theoretical approaches discussed below differ in their treatment of the $3d_{z^2}$ sector and its role in pairing, as summarized in table 2.

6.1. Localized and itinerant regimes of the $3d_{z^2}$ sector

The role of the γ band is one of the central questions in the SC of bilayer nickelates [40, 91, 94, 97]. In the Hund-assisted picture, the essential assumption is that the $3d_{z^2}$ sector retains substantial local-moment character and sizable interlayer AFM correlations on the energy scale relevant to pairing [129, 167]. Its appropriate low-energy description is determined by the coherent spectral weight and magnetic response of this sector.

In a localized regime, the γ band can remain below E_F while the $3d_{z^2}$ sector retains local moments and rung correlations. A shallow γ pocket with small coherent weight is also compatible with an orbital-selective metallic regime in which these magnetic correlations persist. The Hund-assisted scenario can accommodate either situation.

When the γ pocket becomes sizable and coherent and the $3d_{z^2}$ band is only weakly renormalized, the $3d_{z^2}$ quasiparticles must be retained as active low-energy degrees of freedom. An itinerant two-orbital description is then appropriate because these states may participate directly in pairing through hybridization with the $3d_{x^2-y^2}$ states. Rung-singlet correlations may remain relevant over part of this localized-to-itinerant crossover. The single-orbital projection becomes less controlled as the coherent $3d_{z^2}$ weight grows and its magnetic response weakens.

Joint measurements of the $3d_{z^2}$ spectral weight and interlayer magnetic response in the superconducting high-pressure phase would locate the material within this crossover and constrain the appropriate low-energy description.

6.2. Weak- and intermediate-coupling approaches

In itinerant approaches, the starting point is the multiorbital Fermi surface obtained from DFT or a renormalized tight-binding/DMFT description. On-site interactions are treated within weak- and intermediate-coupling scheme such as RPA, FLEX, and functional renormalization group, and the leading pairing instability is obtained from the linearized gap equation. Pairing is mediated by momentum-dependent spin and orbital fluctuations of the itinerant quasiparticles [118, 119, 128, 161]. The leading pairing state depends sensitively on the model parameters, and these calculations commonly find close competition among sign-changing extended-s ($s_{\pm}$), d_{xy}, and $d_{x^2-y^2}$ eigenfunctions.

The same extended-s representation can therefore arise from different microscopic structures. In itinerant theories, its sign structure is selected by scattering between Fermi-surface sheets and can involve a coherent γ pocket. In the localized-rung theory, the primary pairing object is the interlayer singlet operator. Orbital-resolved gap signs and the bilayer magnetic response can distinguish these two limits.

In a conventional weak-coupling framework, the predicted T_c is primarily governed by the DOS N_F at the Fermi level and the effective interaction strength g, following the effective relation approximately $T_c \propto \mathrm{e}^{-1/(gN_F)}$. Increasing hopping integral t broadens the electronic bands and reduces N_F. Furthermore, within the RPA framework, the effective pairing vertex g is proportional to the bare susceptibility, which is inversely related to the bandwidth. As the bands broaden, both N_F and the effective interaction are suppressed, predicting a decrease in T_c. Perturbative calculations typically employ a screened effective U chosen within the regime where the approximation remains controlled. In the strong-coupling limit, the pairing mechanism shifts from a DOS-driven process to one dictated by local magnetic superexchange. Here, the pairing strength is primarily determined by the effective interlayer superexchange $J_{\perp}$ [5, 243], which scales as t^2/U [129, 143].

Rare-earth substitution provides a useful comparison between weak- and strong-coupling calculations. For the high-pressure $R_3Ni_2O_7$ series, calculations reveal an increasing in the bandwidth W and a decrease in the effective interaction ratio U/W as the rare-earth ionic radius decreases. In the specific RPA calculations, this trend weakens the leading $s_{\pm}$ pairing instability [136, 218]. The corresponding pairing scale is therefore predicted to decrease from La toward the smaller rare-earth ions. In the strong-coupling reduction, the same increase of the hopping amplitudes produces larger exchange scales, $J \sim 4t^2/U$, and enhances the calculated interlayer pairing strength [143, 218]. The different trends reflect the distinct low-energy scales controlling pairing in the two calculations. A quantitative comparison also depends on the electronic structure and exchange parameters of each substituted compound.

6.3. Alternative local strong-coupling constructions

Given the structural and electronic similarities between bilayer nickelates and cuprates, a persistent question is whether their high-T_c superconducting mechanisms are fundamentally alike [166, 171]. Both systems feature strongly correlated two-dimensional transition-metal oxide planes and exhibit certain comparable Fermi surface topologies. This physical similarity motivates theoretical scenarios that treat $La_3Ni_2O_7$ as a bilayer cuprate analog whose low-energy physics is governed mainly by the hybridized Ni $3d_{x^2-y^2}$ and in-plane O $2p$ orbitals.

Drawing upon this cuprate-like perspective, a scenario in [171] proposed that the robust interlayer coupling of the $3d_{z^2}$ orbitals and the strong intralayer hybridization of the $3d_{x^2-y^2}$ orbitals collectively suppress the effective Hund's coupling. This decouples the Ni $3d_{z^2}$ orbital from the active pairing mechanism. Instead, the pressure-induced $3d_{z^2}$-dominated γ-band acts primarily as a self-doping charge reservoir. By accommodating excess holes under pressure, it effectively tunes the active $3d_{x^2-y^2}$ bands toward near-optimal doping. Mapping the system onto an effective bilayer t–$t_{\perp}$–J model reveals that the pairing originates from the conventional intralayer AFM exchange [171]. Specifically, the near-optimally doped β band primarily drives the high-T_c d-wave state, while the heavily overdoped α band, resulting from strong bilayer splitting, contributes an additional s-wave component. This inter-band interplay can stabilize a mixed time-reversal-symmetry-breaking $d+is$ pairing symmetry.

Emphasizing the role of strong interlayer coupling, another theoretical approach treats the bilayer system in the basis of molecular bonding and antibonding bands, proposing a self-doped molecular Mott insulator mechanism [135, 196, 222, 226]. In this scenario, the large Hubbard repulsion U drives two nearly degenerate antisymmetric molecular orbitals (derived from $3d_{z^2}$ and $3d_{x^2-y^2}$ states) into a two-orbital molecular Mott insulator limit. The unique feature of this model is its intrinsic self-doping mechanism. A fraction of electrons transfers into the slightly higher-energy symmetric $3d_{x^2-y^2}$ band. This partial occupation effectively leaves doped holes within the strongly correlated antisymmetric orbitals, establishing a physical picture closely analogous to hole-doped cuprates. SC then emerges directly from the electronic correlations within this self-doped background. While intraorbital interactions naturally favor a cuprate-like d-wave pairing, the model demonstrates that strong interorbital effects can overcome

this tendency to stabilize an extended *s*-wave state, offering a distinct molecular-orbital perspective on the pairing mechanism.

A related two-component strong-coupling framework highlights the synergistic roles of the two active E_g orbitals [126, 134, 138, 200]. Driven by strong on-site Coulomb repulsion, the $3d_{z^2}$ states are effectively localized, forming interlayer spin singlets via a robust *c*-axis superexchange interaction. Macroscopic SC emerges when these localized singlets hybridize with the itinerant, nearly quarter-filled in-plane $3d_{x^2-y^2}$ metallic bands. This interorbital hybridization mobilizes the local pairs to establish global phase coherence, yielding a multi-band extended *s*-wave gap structure. Auxiliary-field Monte Carlo simulations reveal that this hybridization plays a fundamental dual role [138]. While it provides the necessary kinetic pathways for phase coherence, excessive hybridization eventually disrupts the local singlet formation itself. The calculated pairing strength becomes nonmonotonic as the hybridization increases. This trend may be relevant to the superconducting dome observed under pressure. Furthermore, these numerical results demonstrate that the calculated maximum T_c scales roughly linearly with the interlayer superexchange *J*, suggesting that the pairing strength could be further optimized through targeted uniaxial *c*-axis compression.

Alternatively, DMFT studies provide a strongly correlated multiorbital description [139, 156, 173, 189]. Cluster-DMFT calculations of the normal state find a non-Fermi-liquid regime in which Hund's coupling transfers the interlayer AFM correlations of the $3d_{z^2}$ sector to the $3d_{x^2-y^2}$ sector [173]. At low pressure, a fully occupied $3d_{z^2}$ bonding state supports strong interlayer AFM correlations and a short-range SDW tendency. Pressure shifts this state toward E_F, weakens the static SDW tendency, and enhances quasiparticle coherence, while sizable local spin fluctuations remain relevant [173, 189]. Separate DMFT calculations of the superconducting state find concomitant $s_\pm$-wave pairing in both E_g orbitals, coupled through interorbital hopping and Hund's interaction [139]. These calculations provide another cooperative multiorbital scenario in which Hund's coupling links the magnetic and pairing correlations of the two E_g sectors.

6.4. Experimental tests and distinguishing criteria

The gap structure probes the superconducting state predicted by a theory. Magnetic and spectral measurements determine whether its assumed low-energy degrees of freedom are realized. Because the electronic structure varies appreciably from sample to sample, these measurements are most informative when performed on the same superconducting specimens.

Recent ARPES and STM studies on superconducting films report nodeless gaps on several Fermi-surface sheets [93, 95, 105, 107, 110]. High-pressure point-contact and Andreev-reflection measurements give different indications for the bulk gap symmetry [66, 69]. Low-temperature penetration-depth and thermal-transport measurements would establish whether symmetry-protected nodes are present.

Proposed superconducting pairings include the intralayer *d*-wave and interlayer *s*-wave states. The nodal *d*-wave pairing state would point to an intralayer-dominated pairing regime, whereas the observed nodeless gaps are compatible with the interlayer *s*-wave pairings [93,95,105,107,110]. The gaps on the α/β and γ sheets along the Brillouin-zone diagonals selectively probe the character of the intrinsic pairing orbitals: If the interlayer pairing resides intrinsically in the $3d_{z^2}$ orbital, then the α/β gaps are induced primarily through orbital hybridization and the nodes or near-nodes appear along the Brillouin-zone diagonals [231]. This is difficult to reconcile with the finite, nearly isotropic gaps observed in experiments [93,112]. The interlayer *s*-wave pairing state dominated by the intrinsic $3d_{x^2-y^2}$-orbital pairing can instead reproduce the nearly isotropic, nodeless gaps [231]. In this case, the diagonal gaps in the bonding and antibonding α/β sectors satisfy $\Delta_\alpha(\mathrm{k}_{diag}) = -\Delta_\beta(\mathrm{k}_{diag})$, providing a concrete target for phase-sensitive measurements.

Mirror-selective quasiparticle interference and the response to controlled nonmagnetic disorder are also sensitive to the sign structure between the bonding and antibonding bands [165, 195]. Thin-film Josephson geometries that couple differently to the two bilayer combinations could provide a more direct measurement of their relative phase. Electronic Raman scattering provides complementary information on the gap scales, anisotropy, and nodal low-energy power laws [221, 227].

The bilayer parity of the spin response offers another distinction. For bonding-antibonding $s_\pm$ pairing, calculations predict a spin resonance mainly in the odd (layer-antisymmetric) channel near the *X* point. A *d*-wave state produces resonances in both the even and odd spin channels [164]. Normal-state RIXS and INS measurements have already established sizable interlayer magnetic correlations in bulk crystals and strained films [47, 53, 92]. Following the parity-resolved response across T_c and under controlled tuning would show whether the pairing scale develops together with rung magnetism. A common evolution of the odd-spin-channel spectral weight and the pairing scale would be consistent with a

rung-mediated interaction. Strong SC accompanied by a weak odd-spin-channel response would favor an itinerant multiorbital description with a smaller contribution from local rung exchange.

Orbital-selective pseudogap calculations associate a loss of low-energy $3d_{z^2}$ spectral weight with rung correlations above the onset of global phase coherence [167]. Temperature-dependent ARPES, together with NMR and optical or terahertz measurements, can follow this proposed sequence [38, 55, 99, 105, 107].

The γ band should be characterized together with the bilayer magnetic response on the same superconducting samples. ARPES measurements on superconducting films place this band either across E_F as a shallow pocket or below E_F, depending on the sample [30, 91, 94, 97, 107]. The relevant distinction is set by its coherent spectral weight and accompanying magnetic response, in addition to its position relative to E_F. A shallow pocket with small coherent weight can coexist with local moments and rung correlations. A coherent and weakly renormalized γ sheet identifies a more itinerant regime in which the $3d_{z^2}$ quasiparticles must be retained explicitly. Combining ARPES with parity-resolved magnetic measurements under the same tuning conditions would locate the material within this local-to-itinerant crossover. Tracking a possible Lifshitz crossing would further show whether changes in T_c correlate more closely with the γ-band topology or with the interlayer magnetic response.

No single observation uniquely identifies the Hund-assisted mechanism. A more discriminating test is their joint occurrence on the same superconducting sample: a strongly renormalized $3d_{z^2}$ sector, sizable interlayer spin correlations, and a dominant interlayer pairing in the $3d_{x^2-y^2}$ orbitals.

7. Comparison with other materials

The single-layer Ruddlesden-Popper compounds R_2NiO_4 and Ca_2RuO_4 offer a broader perspective on the relation between lattice control and correlated electronic states. Both adopt the $n = 1$ K_2NiF_4-type structure, in which individual transition-metal-oxide sheets are separated by rock-salt layers [244, 245]. Their geometry is therefore closer to that of single-layer cuprates than to the NiO_2 bilayer of $La_3Ni_2O_7$. At a more general level, Hund coupling may allow spin correlations concentrated in one orbital sector to influence carriers in another [246]. $La_3Ni_2O_7$ gives a particularly transparent setting for this process, since the $3d_{z^2}$ orbitals form a strongly coupled rung while the $3d_{x^2-y^2}$ states remain more dispersive within the planes [40, 47, 53]. This bilayer geometry provides a natural setting for rung pairing in Hund-assisted models. The nominal filling and lattice distortions also differ between these materials and $La_3Ni_2O_7$, which further modifies their low-energy electronic structures.

No superconducting phase has yet been established in the $n = 1$ nickelates R_2NiO_4. High-pressure transport measurements found no superconducting transition in La_2NiO_4 up to 50 GPa [39]. In Sr-substituted $La_{2-x}Sr_xNiO_4$, no SC was detected down to 30 mK even in the most conductive compositions [247]. The single-layer structure contains no inner-apical Ni–O–Ni rung and hence no large intra-bilayer $3d_{z^2}$ bonding-antibonding splitting or short-rung exchange $J_\perp$. The nominal Ni^{2+} configuration is close to d^8, in contrast to the average $d^{7.5}$ filling of $La_3Ni_2O_7$ [244]. In doped La_2NiO_4, the added holes are strongly involved in charge and spin stripe correlations, and a coherent low-temperature metal is difficult to stabilize [248, 249]. The known $n = 1$ phase diagram is therefore governed by a different balance of itinerancy and magnetic correlations from that of the bilayer compound. Should an orbitally differentiated metallic state be reached, Hund coupling could still connect correlations in the two e_g sectors. Recent developments in nickelates motivate renewed exploration of this possibility in coherently strained films and artificial interfaces, where the local structure and carrier density can be tuned together [86, 250].

Ca_2RuO_4 provides a complementary $n = 1$ example in a $4d$ oxide. At ambient pressure, distortions of the RuO_6 octahedra stabilize a spin-one Mott-insulating state [245, 251]. Pressure suppresses the insulating phase and produces a metallic state [252]. Above approximately 9 GPa, weak resistive and ac-susceptibility anomalies near 0.4 K have been interpreted as signatures of superconductivity [253]. Epitaxial strain also converts Ca_2RuO_4 films into a metallic state [254, 255]. Separately, SC has been reported in Ca_2RuO_4 nanofilm crystals [256]. These experiments establish a close connection between lattice relaxation and electronic itinerancy, while the superconducting state is still being characterized. In Ca_2RuO_4, orbital differentiation develops within the Ru t_{2g} manifold of a single RuO_2 sheet, with spin–orbit coupling playing an important role. Hund coupling may influence the evolution of these orbital correlations as metallic coherence develops [246]. The resulting correlations are organized within a single RuO_2 sheet and have a spatial structure distinct from the $3d_{z^2}$ rung channel of the bilayer nickelate. Their electronic band structure and magnetic behavior are also different.

The comparison between $n = 1$ compounds and $La_3Ni_2O_7$ places the latter in a distinctive position within the broader family of structure-controlled correlated oxides. A key feature of the bilayer nickelate is that straightening the inner-apical Ni–O–Ni bond strengthens both the effective hopping between $3d_{z^2}$-orbitals along the rung and the associated interlayer magnetic exchange [21, 47, 53, 89]. In the Hund-assisted scenario, Hund coupling transfers these interlayer correlations to the more itinerant $3d_{x^2-y^2}$ carriers, thereby providing a natural channel for interlayer *s*-wave pairing. This bilayer geometry, and the associated interlayer pairing channel, is generally absent in the $n = 1$ compounds.

Structural optimization therefore acquires a specific microscopic consequence in $La_3Ni_2O_7$, while Hund coupling may connect the resulting rung correlations to the more itinerant orbital sector. At present, no available experiment uniquely establishes the Hund-assisted microscopic mechanism. The simultaneous observation of the spectral, magnetic, and gap signatures would support the local-rung interlayer-pairing mechanism and enable a sharper comparison with alternative mechanisms. Studies across higher-layer Ruddlesden-Popper nickelates and layer-controlled heterostructures may follow how this interlayer channel evolves with layer number [30, 250, 257, 258]. Multilayer cuprates provide a further reference for understanding how interlayer exchange enters a superconducting state [171, 259].

8. Summary and discussion

High-T_c SC has now been reported in pressurized bulk bilayer nickelates and in strained thin films at ambient pressure. In both settings, SC is closely associated with changes in the local structure. Available spectroscopy reveals pronounced orbital differentiation, and magnetic measurements establish sizable bilayer correlations. Bulk and film studies provide complementary information, with several results remaining sample dependent. Normal-state measurements also show pronounced correlation effects and competing order. The coherence of the γ sector in superconducting samples and the pairing symmetry remain open questions.

This review has focused on a family of strong-coupling theories built around Hund's coupling. They share a common starting point in which the two E_g orbitals play different low-energy roles. In this construction, the $3d_{z^2}$ orbital has strong interlayer hopping and lies close to a local-moment regime, whereas the itinerant $3d_{x^2-y^2}$ band carries mobile in-plane charge. AFM superexchange across an inner-apical rung gives the $3d_{z^2}$ spins a large interlayer scale. On each Ni site, J_H aligns the $3d_{z^2}$ and $3d_{x^2-y^2}$ spins. In the localized and strong-Hund limit, the rung exchange can then be projected into an effective interlayer interaction between the mobile $3d_{x^2-y^2}$ carriers. Minimal single-orbital bilayer calculations commonly find an interlayer spin-singlet state with interlayer *s*-wave symmetry. When the intralayer channel grows, *d* and mixed $s + id$ states can compete.

The role of the γ band gives important insight for the pairing mechanism. A shallow γ pocket with small quasiparticle weight can coexist with local-spin correlations and can be included in a two-orbital Hund model. A large and coherent γ sheet instead requires an itinerant multiorbital description and makes the single-orbital projection unreliable. Pressure and strain also change more than the interlayer exchange. Structural tuning modifies several microscopic parameters at the same time. The association between SC and a straighter inner-apical bond places the bilayer rung among the important ingredients. The combination of microscopic parameters controlling SC remains unsettled.

An additional feature of the normal state is the pseudogap-like spectral weight suppression observed in several experiments. Some strong-coupling calculations associate the loss of coherent $3d_{z^2}$ spectral weight above the phase-coherent superconducting state with strong interlayer correlations and pairing fluctuations. Such a scenario provides a possible connection between the normal-state pseudogap and the interlayer pairing channel discussed here. However, the existing pseudogap-like observations do not by themselves establish the orbital origin or the microscopic pairing mechanism. Further momentum-resolved measurements of the $3d_{z^2}$ spectral weight above T_c will be important for clarifying its relation to superconductivity.

Other theories start from different limits of the same multiorbital system. Weak- and intermediate-coupling approaches pair coherent Fermi-surface sheets through momentum-dependent spin fluctuations. Cuprate-like strong-coupling models place the main pairing interaction in the $3d_{x^2-y^2}$ sector and use the γ band mainly as a charge reservoir. Molecular-orbital and hybridization-based models keep both orbitals active but assign a different role to local rung singlets. These approaches can produce extended-*s*, *d*, or mixed states for different reasons. The same gap representation can therefore arise from different microscopic pairing processes. Lattice effects may further renormalize these electronic mechanisms, and their quantitative contribution to pairing remains open.

Future measurements should determine the band dependence and relative signs of the superconducting gaps. Bilayer-resolved magnetic probes can test whether the pairing scale follows the interlayer spin response. Spectral measurements of the γ band and the orbital content of the superfluid response can then locate the system within the local-to-itinerant crossover of the $3d_{z^2}$-orbital. Tracking these quantities under controlled tuning is more informative than comparing isolated measurements from different samples. Progress requires comparing trends measured on well-characterized samples with the parameter regime in which each reduced model applies. Measurements performed on the same superconducting samples will be especially valuable for distinguishing the proposed pairing mechanisms.

Acknowledgments

C.W. is supported by the National Natural Science Foundation of China under the Grants Nos. 12234016, 12574274 and 12550402. F.Y. is supported by the National Natural Science Foundation of China under the Grant Nos. 12574141. Z.P. is supported by the National Natural Science Foundation of China under Grant No. 12504219 and the startup funding from Xiamen University. C.L. is supported by the National Natural Science Foundation of China under the Grants No. 12304180. This work has been supported by the New Cornerstone science Foundation. This work was supported by the CAS Superconducting Research Project under Grant No. [SCZX-0101].

Data availability statement

The data cannot be made publicly available upon publication because no suitable repository exists for hosting data in this field of study. The data that support the findings of this study are available upon reasonable request from the authors.

Author contributions

Zhiming Pan 0009-0009-8713-3239
Writing – original draft (equal), Writing – review & editing (equal)

Chen Lu
Writing – original draft (equal), Writing – review & editing (equal)

Fan Yang
Writing – original draft (equal), Writing – review & editing (equal)

Congjun Wu 0000-0001-5191-6869
Writing – original draft (equal), Writing – review & editing (equal)

References

[1] Bednorz J G and Müller K A 1986 Possible highT_c superconductivity in theBa-La-Cu-O system *Phys. B Condens. Matter* **64** 189
[2] Anderson P W 1987a The resonating valence bond state in la2cuo4 and superconductivity *science* **235** 1196
[3] Tsuei C and Kirtley J 2000 Pairing symmetry in cuprate superconductors, 69 *Rev. Mod. Phys.* **72** 969
[4] Damascelli A, Hussain Z and Shen Z-X 2003 Angle-resolved photoemission studies of the cuprate superconductors *Rev. Mod. Phys.* **75** 473
[5] Lee P A, Nagaosa N and Wen X-G 2006 Doping a mott insulator: Physics of high-temperature superconductivity *Rev. Mod. Phys.* **78** 17
[6] Armitage N, Fournier P and Greene R 2010 Progress and perspectives on electron-doped cuprates *Rev. Mod. Phys.* **82** 2421
[7] Taillefer L 2010 Scattering and pairing in cuprate superconductors *Annu. Rev. Condens. Matter Phys.* **1** 51
[8] Keimer B, Kivelson S A, Norman M R, Uchida S and Zaanen J 2015 From quantum matter to high-temperature superconductivity in copper oxides *Nature* **518** 179
[9] Proust C and Taillefer L 2019 The remarkable underlying ground states of cuprate superconductors, Annu *Rev. Condens. Matter Phys.* **10** 409
[10] Zhang J, Wu H, Zhao G, Han L and Zhang J 2022 A review on strain study of cuprate superconductors *Nanomaterials* **12** 3340
[11] Zhang Z, Greenblatt M and Goodenough J 1994 Synthesis, structure and properties of the layered perovskite $La_3Ni_2O_{7-\delta}$ *J. Solid State Chem.* **108** 402
[12] Anisimov V I, Bukhvalov D and Rice T M 1999 Electronic structure of possible nickelate analogs to the cuprates *Phys. Rev. B* **59** 7901
[13] Lee K-W and Pickett W 2004 Infinite-layer $LaNiO_2$:Ni^1+ is notCu^2+ *Phys. Rev. B* **70** 165109

[14] Pardo V and Pickett W E 2011 Metal-insulator transition in layered nickelates $La_3Ni_2O_{7-\delta}$ ($\delta = 0.0, 0.5, 1$) *Phys. Rev. B* **83** 245128
[15] Nakata M, Ogura D, Usui H and Kuroki K 2017 Finite-energy spin fluctuations as a pairing glue in systems with coexisting electron and hole bands *Phys. Rev. B* **95** 214509
[16] Li D, Lee K, Wang B Y, Osada M, Crossley S, Lee H R, Cui Y, Hikita Y and Hwang H Y 2019 Superconductivity in an infinite-layer nickelate *Nature* **572** 624
[17] Kitamine N, Ochi M and Kuroki K 2020 Designing nickelate superconductors with d^8 configuration exploiting mixed-anion strategy *Phys. Rev. Res.* **2** 042032
[18] Botana A S, Bernardini F and Cano A 2021 Nickelate superconductors: an ongoing dialog between theory and experiments *J. Exp. Theor. Phys.* **132** 618
[19] Nomura Y and Arita R 2022 Superconductivity in infinite-layer nickelates *Rep. Prog. Phys.* **85** 052501
[20] Liu Z *et al* 2023a Evidence for charge and spin density waves in single crystals of $La_3Ni_2O_7$ and $La_3Ni_2O_6$ *Sci. China-Phys. Mech. Astron.* **66** 217411
[21] Sun H *et al* 2023 Signatures of superconductivity near 80k in a nickelate under high pressure *Nature* **621** 493
[22] Hou J *et al* 2023 Emergence of high-temperature superconducting phase in pressurized $La_3Ni_2O_7$ crystals *Chin. Phys. Lett.* **40** 117302
[23] Wang G *et al* 2024a Pressure-induced superconductivity in polycrystalline $La_3Ni_2O_{7-\delta}$ *Phys. Rev. X* **14** 011040
[24] Zhang Y *et al* 2024a High-temperature superconductivity with zero resistance and strange-metal behaviour in $La_3Ni_2O_{7-\delta}$ *Nat. Phys.* **20** 1269
[25] Ko E K *et al* 2025 Signatures of ambient pressure superconductivity in thin film $La_3Ni_2O_7$ *Nature* **638** 935
[26] Zhou G *et al* 2025a Ambient-pressure superconductivity onset above 40 k in (La, Pr) $_3Ni_2O_7$ films *Nature* **640** 641
[27] Liu Y *et al* 2025a Superconductivity and normal-state transport in compressively strained $La_2PrNi_2O_7$ thin films *Nat. Mater.* **24** 1221–7
[28] Hao B *et al* 2025 Superconductivity in sr-doped $La_3Ni_2O_7$ thin films *Nat. Mater.* **24** 1756
[29] Wang M, Hao B, Sun W, Yan S, Sun S, Zhang H, Gu Z and Nie Y 2026a Superconducting dome in $La_{3-x}Sr_xNi_2O_{7-\delta}$ thin films *Phys. Rev. Lett.* **136** 066002
[30] Nie Z *et al* 2026 Superconductivity and electronic structures of nickelate thin film superstructures *Nature* **652** 628–34
[31] Qiu Z *et al* 2026 High-temperature superconductivity at 100 k in $La_{3-x}Nd_xNi_2O_7$ *Nat. Commun.* **17** 9675
[32] Li F *et al* 2026a Bulk superconductivity up to 96 k in pressurized nickelate single crystals *Nature* **649** 871
[33] Zhou G *et al* 2026a Superconductivity onset above 60k in ambient-pressure nickelate films *Nat. Sci. Rev.* **13** nwag151
[34] Wang N, Wang G, Shen X, Hou J, Luo J, Ma X, Yang H, Shi L, Dou J and Feng J *et al* 2024b Bulk high-temperature superconductivity in pressurized tetragonal $La_2PrNi_2O_7$ *Nature* **634** 579
[35] Li J *et al* 2025 Identification of superconductivity in bilayer nickelate $La_3Ni_2O_7$ under high pressure up to 100 GPa *Natl. Sci. Rev.* **12** nwaf220
[36] Liu L, Guo J, Hu D, Yan G, Chen Y, Yu L, Wang M, Liu X-D and Huang X 2025b Evidence for the meissner effect in the nickelate superconductor La_3Ni_2o7-δ single crystal using diamond quantum sensors *Phys. Rev. Lett.* **135** 096001
[37] Zhong Q *et al* 2026a Evolution of superconductivity evidence in pressurized $La_3 - xsm_xNi_2O_7$ *Phys. Rev. B* **113** 174512
[38] Liu Z *et al* 2024a Electronic correlations and partial gap in the bilayer nickelate $La_3Ni_2O_7$ *Nat. Commun.* **15** 7570
[39] Zhang M, Pei C, Wang Q, Zhao Y, Li C, Cao W, Zhu S, Wu J and Qi Y 2024b Effects of pressure and doping on ruddlesden-popper phases$La_n + 1Ni_nO_3n + 1$ *J. Mater. Sci. Technol.* **185** 147
[40] Yang J *et al* 2024a Orbital-dependent electron correlation in double-layer nickelate $La_3Ni_2O_7$ *Nat. Commun.* **15** 4373
[41] Kakoi M *et al* 2024a Multiband metallic ground state in multilayered nickelates $La_3Ni_2O_7$ and $La_4Ni_3O_10$ probed by ^{139}la-nmr at ambient pressure *J. Phys. Soc. Japan* **93** 053702
[42] Li Y *et al* 2025b Distinct ultrafast dynamics of bilayer and trilayer nickelate superconductors regarding the density-wave-like transitions *Sci. Bull.* **70** 180
[43] Wang L *et al* 2024c Structure responsible for the superconducting state in $La_3Ni_2O_7$ at high-pressure and low-temperature conditions *J. Am. Chem. Soc.* **146** 7506
[44] Zhou Y *et al* 2025b Investigations of key issues on the reproducibility of high-t_c superconductivity emerging from compressed $La_3Ni_2O_7$ *Matter Radiat. Extremes* **10** 027801
[45] Dong Z *et al* 2024 Visualization of oxygen vacancies and self-doped ligand holes in $La_3Ni_2O_{7-\delta}$ *Nature* **630** 847
[46] Chen X *et al* 2024a Polymorphism in the ruddlesden-popper nickelate $La_3Ni_2O_7$: discovery of a hidden phase with distinctive layer stacking *J. Am. Chem. Soc.* **146** 3640
[47] Chen X *et al* 2024b Electronic and magnetic excitations in $La_3Ni_2O_7$ *Nat. Commun.* **15** 9597
[48] Zhao D *et al* 2025 Pressure-enhanced spin-density-wave transition in double-layer nickelate $La_3Ni_2O_{7-\delta}$ *Sci. Bull.* **70** 1239–45
[49] Abadi S *et al* 2025 Electronic structure of the alternating monolayer-trilayer phase of $La_3Ni_2O_7$ *Phys. Rev. Lett.* **134** 126001
[50] Wang H, Chen L, Rutherford A, Zhou H and Xie W 2024d Long-range structural order in a hidden phase of ruddlesden-popper bilayer nickelate $La_3Ni_2O_7$ *Inorg. Chem.* **63** 5020
[51] Liu Z *et al* 2025c Evolution of electronic correlations in the ruddlesden-popper nickelates *Phys. Rev. B* **111** L220505
[52] Plokhikh I *et al* 2026 Unraveling spin density wave order in layered nickelates $La_3Ni_2O_7$ and $La_2PrNi_2O_7$ via neutron diffraction *Phys. Rev. Res.* **8** 033151
[53] Xie T *et al* 2024 Strong interlayer magnetic exchange coupling in $La_3Ni_2O_{7-\delta}$ revealed by inelastic neutron scattering *Sci. Bull.* **69** 3221
[54] Meng Y *et al* 2024 Density-wave-like gap evolution in $La_3Ni_2O_7$ under high pressure revealed by ultrafast optical spectroscopy *Nat. Commun.* **15** 10408
[55] Li Y *et al* 2024a Electronic correlation and pseudogap-like behavior of high-temperature superconductor $La_3Ni_2O_7$ *Chin. Phys. Lett.* **41** 087402
[56] Wang G *et al* 2025a Chemical versus physical pressure effects on the structure transition of bilayer nickelates, *npj Quantum Mater.* **10** 1
[57] Li M *et al* 2024b Distinguishing electronic band structure of single-layer and bilayer ruddlesden-popper nickelates probed by in-situ high pressure x-ray absorption near-edge spectroscopy (arXiv:2410.04230)
[58] Zhou X *et al* 2024 Revealing nanoscale structural phase separation in $La_3Ni_2O_{7-\delta}$ single crystal via scanning near-field optical microscopy (arXiv:2410.06602)

[59] Su B, Huang C, Zhao J, Huo M, Luo J, Wang M and Chen Z-G 2024 Strongly anisotropic charge dynamics in $La_3Ni_2O_7$ with coherent-to-incoherent crossover of interlayer charge dynamics (arXiv:2411.10786)
[60] Mijit E *et al* 2024 Local electronic properties of $La_3Ni_2O_7$ under pressure (arXiv:2412.08269)
[61] Chen B *et al* 2025a Unveiling the multiband metallic nature of the normal state in the nickelate $La_3Ni_2O_7$ *Phys. Rev. B* **111** 054519
[62] Shi M *et al* 2025a Spin density wave rather than tetragonal structure is prerequisite for superconductivity in $La_3Ni_2O_{7-\delta}$ *Nat. Commun.* **16** 9141
[63] Huo M, Ma P, Huang C, Huang X, Sun H and Wang M 2025a Low volume fraction of high-tc superconductivity in $La_3Ni_2O_7$ at 80 k and ambient pressure (arXiv:2501.15929)
[64] Li M *et al* 2025c Orbital signatures of density wave transition in $La_3Ni_2O_7$-delta and $La_2PrNi_2O_7$-delta rp-nickelates probed via in-situ x-ray absorption near-edge spectroscopy (arXiv:2502.10962)
[65] Yashima M, Seto N, Oshita Y, Kakoi M, Sakurai H, Takano Y and Mukuda H 2025 Microscopic evidence for spin-spinless stripe order with reduced ni moments within ab plane for bilayer nickelate $La_3Ni_2O_7$ probed by 139la-nqr *J. Phys. Soc. Japan* **94** 054704
[66] Guo J, Chen Y, Wang Y, Sun H, Hu D, Wang M, Huang X and Cui T 2025 Revealing superconducting gap in $La_3Ni_2O_{7-\delta}$ by andreev reflection spectroscopy under high pressure *Nat. Commun.* **16** 10838
[67] Dong Z, Wang G, Wang N, Dong W-H, Gu L, Xu Y, Cheng J, Chen Z and Wang Y 2025 Interstitial oxygen order and its competition with superconductivity in $La_2PrNi_2O_{7+\delta}$ *Nat. Mater.* **24** 1927
[68] Wu Q-Y *et al* 2025 Ultrafast optical evidence of coexisting density waves in bilayer nickelate $La_3Ni_2O_7$ *Phys. Rev. B* **112** 235110
[69] Cao Z-Y *et al* 2025 Direct observation of *d*-wave superconducting gap symmetry in pressurized $La_3Ni_2O_7$-delta single crystals (arXiv:2509.12606)
[70] Zhang H *et al* 2025a Identifying the structure of $La_3Ni_2O_7$ in the pressurized superconducting state (arXiv:2511.15265)
[71] Zhang M *et al* 2026a Spin-density-wave transition in monolayer-trilayer $La_3Ni_2O_7$ single crystals *Mater. Today Phys.* **67** 102175
[72] Zhang Y *et al* 2026b Strong oxidizing annealing of bilayer $La_3Ni_2O_{7-\delta}$ results in suppression of superconductivity under high pressure *J. Solid State Chem.* **355** 125757
[73] Shu J *et al* 2026 Contrasting momentum-selective spin-density-wave gaps in bilayer and trilayer nickelates (arXiv:2602.02174)
[74] Gim D-H, Wulferding D, Zhang H, Wang M and Kim K H 2026 Spectroscopic evidence of competing diagonal spin interactions and spin disproportionation in the bilayer nickelate $La_3Ni_2O_7$ (arXiv:2602.05365)
[75] He G *et al* 2026 Anisotropic electronic correlations in the spin density wave state of $La_3Ni_2O_7$ (arXiv:2602.07998)
[76] Gao Y *et al* 2026 Enhancement of metallicity by na doping in $La_3Ni_2O_7 + \delta$ *Phys. Rev. B* **114** L020504
[77] Misawa R *et al* 2026 Polar, checkerboard charge order in bilayer nickelate $La_3Ni_2O_7$ (arXiv:2603.25119)
[78] Chen X *et al* 2026a Dissecting superconductivity in the ruddlesden-popper nickelates: The role of electron correlation and interlayer magnetic exchange (arXiv:2604.01902)
[79] Kriener M *et al* 2026 Controlling the band filling and the band width in nickelate superconductors (arXiv:2604.13875)
[80] Mandyam S *et al* 2026 Uncovering origins of heterogeneous superconductivity in $La_3Ni_2O_7$ *Nature* **651** 54
[81] Chen L *et al* 2026b Nature of magnetism in bilayer nickelate $La_3Ni_2O_7$ single crystals (arXiv:2605.03448)
[82] Korolev A V and Talantsev E F 2026a Nearly twofold overestimation of the superconducting volume fraction in pressurized ruddlesden-popper nickelates (arXiv:2602.19282)
[83] Korolev A V and Talantsev E F 2026b Threefold error in the reported zero-field cooled magnetic moment of single crystal $La_2SmNi_2O_7$ (arXiv:2602.23240)
[84] Liu Z *et al* 2026a Density-wave phases, anisotropic transport, and planckian dissipation in single crystals of the superconductor $La_3Ni_2O_7$ (arXiv:2607.26990)
[85] Sasaki M *et al* 2026 Single-crystal structural phase diagram of stoichiometric bilayer nickelate $La_3Ni_2O_7$ under hydrostatic pressure (arXiv:2607.27607)
[86] Cui T *et al* 2024 Strain-mediated phase crossover in ruddlesden–popper nickelates *Commun. Mater.* **5** 32
[87] Liu Y *et al* 2024b Growth and characterization of the $La_3Ni_2O_{7-\delta}$ thin films: Dominant contribution of the $d_x^2 - y^2$ orbital at ambient pressure *Phys. Rev. Mater.* **8** 124801
[88] Ren X *et al* 2025 Resolving the electronic ground state of $La_3Ni_2O_{7-\delta}$ films *Commun. Phys.* **8** 52
[89] Bhatt L *et al* 2026 Structural modifications in strain-engineered bilayer nickelate thin films *Nature* **653** 1–3
[90] Miao Y *et al* 2025 Electronic structures across superconductor-insulator transition in ruddlesden-popper bilayer nickelate films (arXiv:2502.18068)
[91] Li P *et al* 2025d Angle-resolved photoemission spectroscopy of superconducting $(La,Pr)_3Ni_2O_7/SrLaAlO_4$ heterostructures *Nat. Sci. Rev.* **205** nwaf205
[92] Zhong H *et al* 2025 Spin correlations in $La_3Ni_2O_7$ thin films (arXiv:2502.03178)
[93] Shen J *et al* 2026 Nodeless superconducting gap and electron-boson coupling in (La, Pr, Sm) $_3Ni_2O_7$ films *science* **392** 1396
[94] Wang B Y *et al* 2026b Electronic structure of compressively strained bilayer nickelate thin film *Phys. Rev. X* **16** 031008
[95] Fan S *et al* 2026 Single-particle tunneling spectrum with a robust superconducting gap in $La_2PrNi_2O_7$ thin films at ambient pressure *Sci. Adv.* **12** eaeg2429
[96] Osada M *et al* 2025 Strain-tuning for superconductivity in $La_3Ni_2O_7$ thin films *Commun. Phys.* **8** 251
[97] Sun W *et al* 2026 Observation of superconductivity-induced leading-edge gap in a bilayer nickelate *Nat. Phys.* **22** 1409
[98] Li Q *et al* 2026b Enhanced superconductivity in the compressively strained bilayer nickelate thin films by pressure *Nat. Commun.* **17** 3276
[99] Ji H *et al* 2025a Time-reversal symmetry breaking superconductivity with electronic glass in nickelate (La, Pr, Sm) $_3Ni_2O_7$ films (arXiv:2508.16412)
[100] Xu M *et al* 2026a Coexistence of antiferromagnetic spin fluctuations and superconductivity in $La_2SmNi_2O_7$ thin films (arXiv:2602.07994)
[101] Zhong H *et al* 2026b Doping evolution of spin excitations in $La_{3-x}Sr_xNi_2O_7/SrLaAlO_4$ superconducting thin films (arXiv:2603.01120)
[102] Wang K *et al* 2026c Pauli-limited upper critical field and anisotropic depairing effect of $La_{2.82}Sr_{0.18}Ni_2O_7$ superconducting thin film *Mater. Today* **95** 103269
[103] Liu Y *et al* 2026b A superconducting half-dome in bilayer nickelates (arXiv:2603.12196)
[104] Kumar D, Dans J Z, Avers K E, Paxson R, Takeuchi I and Paglione J 2026 Non-fermi liquid behavior in $La_3Ni_2O_7$ thin films under hydrostatic pressure (arXiv:2603.26978)

[105] Xu S et al 2026b Multimodal terahertz spectroscopy of the pairing symmetry and normal-state pseudogap in $(La,Pr)_3Ni_2O_7$ films (arXiv:2604.04421)
[106] Han Z, Xiang L, Zhou X and Zhu Z 2026 Granular superconductivity in $La_2PrNi_2O_{7-\delta}$ thin films *Chin. Phys. Lett.* **43** 080706
[107] Li Y et al 2026c Three-dimensional electronic structures in superconducting ruddlesden-popper bilayer nickelate films *Phys. Rev. X* **16** 031016
[108] Flavenot M et al 2026 Decoding superconductivity in $La_3Ni_2O_{7-\delta}$ thin films via ozone-driven structure and oxidation tuning (arXiv:2604.09807)
[109] Zhang S et al 2026c Interlayer hybridization enables superconductivity in bilayer nickelates (arXiv:2604.14701)
[110] Liang Z, Wei T, Ren W, Ji H, Xie Z, Liu Y, Wang Z and Wang J 2026 Observation of flat-bottom u-shaped energy gap in high-tc nickelate $(La, Pr)_3Ni_2O_7$ thin films (arXiv:2605.15703)
[111] Wang Z et al 2026d Electron-like high-temperature superconductivity induced by compressive strain in $La_2PrNi_2O_7$ thin films (arXiv:2608.01295)
[112] Miao Y et al 2026 Thermodynamic phase transition, pairing symmetry and fermi surface topology in ruddlesden-popper nickelate films (arXiv:2608.03908)
[113] Qiu W and Yao D-X 2026 Progress of ambient-pressure superconductivity in bilayer nickelate thin films (arXiv:2603.11235)
[114] Wu X, Xiang T and Hu J 2026a Pairing mechanism in bilayer nickelate $La_3Ni_2O_7$ superconductors (arXiv:2604.17181)
[115] Zhang Y, Lin L-F, Maier T A and Dagotto E 2026d Superconductivity in ruddlesden-popper nickelates: a review of recent progress, focusing on thin films (arXiv:2604.18385)
[116] Luo Z, Hu X, Wang M, Wú W and Yao D-X 2023 Bilayer two-orbital model of $La_3Ni_2O_7$ under pressure *Phys. Rev. Lett.* **131** 126001
[117] Zhang Y, Lin L-F, Moreo A and Dagotto E 2023a Electronic structure, dimer physics, orbital-selective behavior and magnetic tendencies in the bilayer nickelate superconductor $La_3Ni_2O_7$ under pressure *Phys. Rev. B* **108** L180510
[118] Yang Q-G, Wang D and Wang Q-H 2023a Possible $S_{\pm}$-wave superconductivity in $La_3Ni_2O_7$ *Phys. Rev. B* **108** L140505
[119] Lechermann F, Gondolf J, Bötzel S and Eremin I M 2023 Electronic correlations and superconducting instability in $La_3Ni_2O_7$ under high pressure *Phys. Rev. B* **108** L201121
[120] Sakakibara H, Kitamine N, Ochi M and Kuroki K 2024 Possible high T_c superconductivity in $La_3Ni_2O_7$ under high pressure through manifestation of a nearly half-filled bilayer hubbard model *Phys. Rev. Lett.* **132** 106002
[121] Gu Y, Le C, Yang Z, Wu X and Hu J 2025 Effective model and pairing tendency in the bilayer ni-based superconductor $La_3Ni_2O_7$ *Phys. Rev. B* **111** 174506
[122] Shen Y, Qin M and Zhang G-M 2023 Effective bi-layer model hamiltonian and density-matrix renormalization group study for the high-T_c superconductivity $La_3Ni_2O_7$ under high pressure *Chin. Phys. Lett.* **40** 127401
[123] Christiansson V, Petocchi F and Werner P 2023 Correlated electronic structure of $La_3Ni_2O_7$ under pressure *Phys. Rev. Lett.* **131** 206501
[124] Shilenko D A and Leonov I V 2023 Correlated electronic structure, orbital-selective behavior and magnetic correlations in double-layer $La_3Ni_2O_7$ under pressure *Phys. Rev. B* **108** 125105
[125] Wú W, Luo Z, Yao D-X and Wang M 2024 Superexchange and charge transfer in the nickelate superconductor $La_3Ni_2O_7$ under pressure *Sci. China-Phys. Mech. Astron.* **67** 117402
[126] Cao Y and Yang Y-f 2024 Flat bands promoted by hund's rule coupling in the candidate double-layer high-temperature superconductor $La_3Ni_2O_7$ under high pressure *Phys. Rev. B* **109** L081105
[127] Chen X, Jiang P, Li J, Zhong Z and Lu Y 2025b Charge and spin instabilities in superconducting $La_3Ni_2O_7$ *Phys. Rev. B* **111** 014515
[128] Liu Y-B, Mei J-W, Ye F, Chen W-Q and Yang F 2023b $s^{\pm}$-wave pairing and the destructive role of apical-oxygen deficiencies in $La_3Ni_2O_7$ under pressure *Phys. Rev. Lett.* **131** 236002
[129] Lu C, Pan Z, Yang F and Wu C 2024a Interlayer-coupling-driven high-temperature superconductivity in $La_3Ni_2O_7$ under pressure *Phys. Rev. Lett.* **132** 146002
[130] Zhang Y, Lin L-F, Moreo A, Maier T A and Dagotto E 2024c Structural phase transition, $s_{\pm}$-wave pairing and magnetic stripe order in bilayered superconductor $La_3Ni_2O_7$ under pressure *Nat. Commun.* **15** 2470
[131] Oh H and Zhang Y-H 2023 Type-II *t–J* model and shared superexchange coupling from hund's rule in superconducting $La_3Ni_2O_7$ *Phys. Rev. B* **108** 174511
[132] Liao Z, Chen L, Duan G, Wang Y, Liu C, Yu R and Si Q 2023 Electron correlations and superconductivity in $La_3Ni_2O_7$ under pressure tuning *Phys. Rev. B* **108** 214522
[133] Qu X-Z, Qu D-W, Chen J, Wu C, Yang F, Li W and Su G 2024 Bilayer $t–j–j_{\perp}$ model and magnetically mediated pairing in the pressurized nickelate $La_3Ni_2O_7$ *Phys. Rev. Lett.* **132** 036502
[134] Yang Y-f, Zhang G-M and Zhang F-C 2023b Interlayer valence bonds and two-component theory for high-T_c superconductivity of $La_3Ni_2O_7$ under pressure *Phys. Rev. B* **108** L201108
[135] Jiang K, Wang Z and Zhang F-C 2024 High temperature superconductivity in $La_3Ni_2O_7$ *Chin. Phys. Lett.* **41** 017402
[136] Zhang Y, Lin L-F, Moreo A, Maier T A and Dagotto E 2023b Trends in electronic structures and $s_{\pm}$-wave pairing for the rare-earth series in bilayer nickelate superconductor $R_3Ni_2O_7$ *Phys. Rev. B* **108** 165141
[137] Huang J, Wang Z D and Zhou T 2023 Impurity and vortex states in the bilayer high-temperature superconductor $La_3Ni_2O_7$ *Phys. Rev. B* **108** 174501
[138] Qin Q and Yang Y-F 2023 High-T_c superconductivity by mobilizing local spin singlets and possible route to higher T_c in pressurized $La_3Ni_2O_7$ *Phys. Rev. B* **108** L140504
[139] Tian Y-H, Chen Y, Wang J-M, He R-Q and Lu Z-Y 2024 Correlation effects and concomitant two-orbital $s_{\pm}$-wave superconductivity in $La_3Ni_2O_7$ under high pressure *Phys. Rev. B* **109** 165154
[140] Lu D-C, Li M, Zeng Z-Y, Hou W, Wang J, Yang F and You Y-Z 2023 Superconductivity from doping symmetric mass generation insulators: application to $La_3Ni_2O_7$ under pressure (arXiv:2308.11195)
[141] Luo Z, Lv B, Wang M, Wú W and Yao D-X 2024 High-t_c superconductivity in $La_3Ni_2O_7$ based on the bilayer two-orbital tj model *npj Quantum Mater.* **9** 61
[142] Zhang J-X, Zhang H-K, You Y-Z and Weng Z-Y 2024d Strong pairing originated from an emergent $\mathbb{Z}_2$ berry phase in $La_3Ni_2O_7$ *Phys. Rev. Lett.* **133** 126501
[143] Pan Z, Lu C, Yang F and Wu C 2024 Effect of rare-earth element substitution in superconducting $R_3Ni_2O_7$ under pressure *Chin. Phys. Lett.* **41** 087401

[144] Lange H, Homeier L, Demler E, Schollwöck U, Bohrdt A and Grusdt F 2024a Pairing dome from an emergent feshbach resonance in a strongly repulsive bilayer model *Phys. Rev. B* **110** L081113

[145] Geisler B, Hamlin J J, Stewart G R, Hennig R G and Hirschfeld P 2024a Structural transitions, octahedral rotations and electronic properties of $A_3Ni_2O_7$ rare-earth nickelates under high pressure *npj Quantum Mater.* **9** 38

[146] Yang H, Oh H and Zhang Y-H 2024b Strong pairing from a small fermi surface beyond weak coupling: application to $La_3Ni_2O_7$ *Phys. Rev. B* **110** 104517

[147] Rhodes L C and Wahl P 2024 Structural routes to stabilize superconducting $La_3Ni_2O_7$ at ambient pressure *Phys. Rev. Mater.* **8** 044801

[148] Lange H, Homeier L, Demler E, Schollwöck U, Grusdt F and Bohrdt A 2024b Feshbach resonance in a strongly repulsive ladder of mixed dimensionality: A possible scenario for bilayer nickelate superconductors *Phys. Rev. B* **109** 045127

[149] Kumar U, Melnick C and Kotliar G 2025 Softening of *dd* excitation in the resonant inelastic x-ray scattering spectra as a signature of hund's coupling in nickelates *Phys. Rev. Res.* **7** L012066

[150] Kaneko T, Sakakibara H, Ochi M and Kuroki K 2024 Pair correlations in the two-orbital hubbard ladder: Implications for superconductivity in the bilayer nickelate $La_3Ni_2O_7$ *Phys. Rev. B* **109** 045154

[151] Ryee S, Witt N and Wehling T O 2024 Quenched pair breaking by interlayer correlations as a key to superconductivity in $La_3Ni_2O_7$ *Phys. Rev. Lett.* **133** 096002

[152] Zhang Y, Lin L-F, Moreo A, Maier T A and Dagotto E 2024e Electronic structure, magnetic correlations and superconducting pairing in the reduced ruddlesden-popper bilayer $La_3Ni_2O_6$ under pressure: different role of $d_3z^2 - r^2$ orbital compared with $La_3Ni_2O_7$ *Phys. Rev. B* **109** 045151

[153] Schlömer H, Schollwöck U, Grusdt F and Bohrdt A 2024 Superconductivity in the pressurized nickelate $La_3Ni_2O_7$ in the vicinity of a BEC-BCS crossover *Commun. Phys.* **7** 366

[154] Chen J, Yang F and Li W 2024c Orbital-selective superconductivity in the pressurized bilayer nickelate $La_3Ni_2O_7$: An infinite projected entangled-pair state study *Phys. Rev. B* **110** L041111

[155] Xia C, Liu H, Zhou S and Chen H 2025 Sensitive dependence of pairing symmetry on ni-eg crystal field splitting in the nickelate superconductor $La_3Ni_2O_7$ *Nat. Commun.* **16** 1054

[156] Ouyang Z, Wang J-M, Wang J-X, He R-Q, Huang L and Lu Z-Y 2024a Hund electronic correlation in $La_3Ni_2O_7$ under high pressure *Phys. Rev. B* **109** 115114

[157] Qu X-Z, Qu D-W, Yi X-W, Li W and Su G 2025 Hund's rule, interorbital hybridization and high-T_c superconductivity in the bilayer nickelate $La_3Ni_2O_7$ *Phys. Rev. B* **112** L161101

[158] Sui X, Han X, Jin H, Chen X, Qiao L, Shao X and Huang B 2024 Electronic properties of the bilayer nickelates $R_3Ni_2O_7$ with oxygen vacancies (R = La orCe) *Phys. Rev. B* **109** 205156

[159] Zheng Y-Y and Wú W 2025 $s_\pm$-wave superconductivity in the bilayer two-orbital hubbard model *Phys. Rev. B* **111** 035108

[160] Kakoi M, Kaneko T, Sakakibara H, Ochi M and Kuroki K 2024b Pair correlations of the hybridized orbitals in a ladder model for the bilayer nickelate $La_3Ni_2O_7$ *Phys. Rev. B* **109** L201124

[161] Heier G, Park K and Savrasov S Y 2024 Competing d_xy and $s_\pm$ pairing symmetries in superconducting $La_3Ni_2O_7$: LDA + FLEX calculations *Phys. Rev. B* **109** 104508

[162] Lechermann F, Bötzel S and Eremin I M 2024 Electronic instability, layer selectivity and fermi arcs in $La_3Ni_2O_7$ *Phys. Rev. Mater.* **8** 074802

[163] Geisler B, Fanfarillo L, Hamlin J J, Stewart G R, Hennig R G and Hirschfeld P 2024b Optical properties and electronic correlations in $La_3Ni_2O_7$ bilayer nickelates under high pressure, *npj Quantum Mater.* **9** 89

[164] Bötzel S, Lechermann F, Gondolf J and Eremin I M 2024 Theory of magnetic excitations in the multilayer nickelate superconductor $La_3Ni_2O_7$ *Phys. Rev. B* **109** L180502

[165] Bötzel S, Lechermann F, Shibauchi T and Eremin I M 2025 Theory of potential impurity scattering in pressurized superconducting $La_3Ni_2O_7$ *Commun. Phys.* **8** 154

[166] Jiang R, Hou J, Fan Z, Lang Z-J and Ku W 2024 Pressure driven fractionalization of ionic spins results in cupratelike high-t_c superconductivity in La_3Ni_2o7 *Phys. Rev. Lett.* **132** 126503

[167] Lu C, Pan Z, Yang F and Wu C 2024b Interplay of two e_g orbitals in superconducting $La_3Ni_2O_7$under pressure *Phys. Rev. B* **110** 094509

[168] Wang Y, Jiang K, Wang Z, Zhang F-C and Hu J 2024e Electronic and magnetic structures of bilayer $La_3Ni_2O_7$ at ambient pressure *Phys. Rev. B* **110** 205122

[169] Oh H, Zhou B and Zhang Y-H 2025 Type-ii t-j model in charge transfer regime in bilayer $La_3Ni_2O_7$ and trilayer $La_4Ni_3O_{10}$ *Phys. Rev. B* **111** L020504

[170] Talantsev E and Chistyakov V 2024 Debye temperature, electron-phonon coupling constant and three-dome shape of crystalline strain as a function of pressure in highly compressed $La_3Ni_2O_{7-\delta}$ *Lett. Mater.* **14** 262

[171] Fan Z, Zhang J-F, Zhan B, Lv D, Jiang X-Y, Normand B and Xiang T 2024 Superconductivity in nickelate and cuprate superconductors with strong bilayer coupling *Phys. Rev. B* **110** 024514

[172] Ouyang Z, Gao M and Lu Z-Y 2024b Absence of electron-phonon coupling superconductivity in the bilayer phase of $La_3Ni_2O_7$ under pressure, *npj Quantum Mater.* **9** 80

[173] Chen Y, Tian Y-H, Wang J-M, He R-Q and Lu Z-Y 2024d Non-fermi liquid and antiferromagnetic correlations with hole doping in the bilayer two-orbital hubbard model of $La_3Ni_2O_7$ at zero temperature *Phys. Rev. B* **110** 235119

[174] Yi X-W, Meng Y, Li J-W, Liao Z-W, Li W, You J-Y, Gu B and Su G 2024 Nature of charge density waves and metal-insulator transition in pressurized $La_3Ni_2O_7$ *Phys. Rev. B* **110** L140508

[175] Liu Y-B, Sun H, Zhang M, Liu Q, Chen W-Q and Yang F 2025d Origin of the diagonal double-stripe spin density wave and potential superconductivity in bulk $La_3Ni_2O_7$ at ambient pressure *Phys. Rev. B* **112** 014510

[176] Zhang H-Y, Bai Y-J, Kong F-J, Wu X-Q, Xing Y-H and Xu N 2024f Doping evolution of the normal state magnetic excitations in pressurized $La_3Ni_2O_7$ *New J. Phys.* **26** 123027

[177] Wu X, Yang H and Zhang Y-H 2024 Deconfined fermi liquid to fermi liquid transition and superconducting instability (arXiv:2401.08753)

[178] Geisler B, Hamlin J J, Stewart G R, Hennig R G and Hirschfeld P J 2025 Fermi surface reconstruction and enhanced spin fluctuations in strained $La_3Ni_2O_7$ on $LaAlO_3(001)$ and $SrTiO_3(001)$ *Phys. Rev. B* **112** L100506

[179] Yue C *et al* 2025 Correlated electronic structures and unconventional superconductivity in bilayer nickelate heterostructures *Nat. Sci. Rev.* **12** nwaf253

[180] Wang Y, Chen Z, Zhang Y, Jiang K and Hu J 2025b The mottness and the anderson localization in bilayer nickelate $La_3Ni_2O_7$ (arXiv:2501.08536)
[181] Shao Z-Y, Liu Y-B, Liu M and Yang F 2025 Band structure and pairing nature of $La_3Ni_2O_7$ thin film at ambient pressure *Phys. Rev. B* **112** 024506
[182] Bhatta H, Zhang X, Zhong Y and Jia C 2025 Structural and electronic evolution of bilayer nickelates under biaxial strain (arXiv:2502.0162)
[183] Shi H, Huo Z, Li G, Ma H, Cui T, Yao D and Duan D 2025b The effect of carrier doping and thickness on the electronic structures of $La_3Ni_2O_7$ thin films *Chin. Phys. Lett.* **42** 080708
[184] Hu X, Qiu W, Chen C-Q, Luo Z and Yao D-X 2025 Electronic structures and multi-orbital models of $La_3Ni_2O_7$ thin films at ambient pressure *Commun. Phys.* **8** 506
[185] Haque M E, Ali R, Masum M, Hassan J and Naqib S 2025 Dft exploration of pressure dependent physical properties of the recently discovered $La_3Ni_2O_7$ superconductor (arXiv:2504.15853)
[186] Huo Z, Zhang P, Shi H, Yan X, Duan D and Cui T 2025b First-principles study of the pr-doped bilayer nickelate $La_3Ni_2O_7$ *Phys. Rev. B* **111** 195118
[187] Yi X-W, Li W, You J-Y, Gu B and Su G 2025 Unifying strain-and pressure-driven superconductivity in $La_3Ni_2O_7$: Suppressed charge and spin density waves and enhanced interlayer coupling *Phys. Rev. B* **112** L140504
[188] Xu H-X and Guterding D 2025 Incommensurate spin fluctuations and competing pairing symmetries in $La_3Ni_2O_7$ *Phys. Rev. B* **112** 174519
[189] Ouyang Z, He R-Q and Lu Z-Y 2025 Phase diagrams and two key factors to superconductivity of ruddlesden-popper nickelates *Phys. Rev. B* **112** 045127
[190] Zhu C, Li B, Fan Y, Yin C, Zhai J, Cheng J, Liu S and Shi Z 2025 Magnetic phases and electron–phonon coupling in $La_3Ni_2O_7$ under pressure *Comput. Mater. Sci.* **250** 113676
[191] Zhao Y-F and Botana A S 2025 Electronic structure of ruddlesden-popper nickelates: Strain to mimic the effects of pressure *Phys. Rev. B* **111** 115154
[192] Lu C, Zhang M, Pan Z, Wu C and Yang F 2025 Impact of pressure and apical oxygen vacancies on superconductivity in $La_3Ni_2O_7$ *Commun. Phys.* **8** 354
[193] You J-Y, Zhu Z, Ben M D, Chen W and Li Z 2025 Unlikelihood of a phonon mechanism for the high-temperature superconductivity in $La_3Ni_2O_7$, *npj Comput. Mater.* **11** 3
[194] Ji J-H, Lu C, Shao Z-Y, Pan Z, Yang F and Wu C 2025b Strong-coupling study of the pairing mechanism in pressurized $La_3Ni_2O_7$ *Phys. Rev. B* **112** 214515
[195] Zhang Z, Zhan J, Le C, Po H C, Hu J and Wu X 2025b Mirror-selective quasiparticle interference in bilayer nickelate superconductor (arXiv:2512.14544)
[196] Wang Z, Zhang H-J, Jiang K and Zhang F-C 2025c Self-doped molecular mott insulator for bilayer high-temperature superconducting $La_3Ni_2O_7$ *Nat. Sci. Rev.* **12** nwaf353
[197] Yang Y, Lu X, Wan Y, Chen W-Q and Gong S-S 2025 Evolution from intralayer to interlayer superconductivity in a bilayer t–j model (arXiv:2507.07545)
[198] Zhu X, Qin W, Cui P and Zhang Z 2026 Quantum phase transition driven by competing intralayer and interlayer hopping in bilayer nickelates *Phys. Rev. B* **113** 075116
[199] Cao Y-H, Jiang K-Y, Lu H-Y, Wang D and Wang Q-H 2026a Strain-engineered electronic structure and superconductivity in $La_3Ni_2O_7$ thin films *Sci. China: Phys. Mech. Astron.* **69** 247412
[200] Wang J and Yang Y-F 2026 Fermi liquid and isotropic superconductivity of hund scenario for bilayer nickelates *npj Quantum Mater.* **11** 39
[201] Chen Z, Liu Y-B and Yang F 2026c Variational monte carlo study on the bilayer t–$j_{\parallel}$–$j_{\perp}$ model for $La_3Ni_2O_7$ *Phys. Rev. B* **113** 174521
[202] Liu L, Peng J, Qiao Z, Cai S, Dong H, Jia Y and Zhang Z 2026c Optimally tensile strained $La_3Ni_2O_7$ films as candidate high-temperature superconductors on designer substrates ba1-xsrxo and sro-terminated srtio3 *Phys. Rev. Lett.* **136** 196002
[203] Wang H-X *et al* 2026e Spin stripes and superconductivity in bilayer nickelates *Phys. Rev. Lett.* **137** 086502
[204] Chen W-Y, Chen C-Q, Wang M, Gong S-S and Yao D-X 2025c Superconductivity of bilayer two-orbital hubbard model for $La_3Ni_2O_7$ under high pressure (arXiv:2511.01801)
[205] Ma R, Fan Z, Ma T and Wu C 2025 Parameter-dependent superconducting transition temperature in a sign-problem-free bilayer model *Chin. Phys. Lett.* **42** 110705
[206] Yang H and Zhang Y-H 2025 Magnetism and superconductivity in bilayer nickelate (arXiv:2512.13793)
[207] Oh H and Zhang Y-H 2025 Pair-density-wave superconductivity and anderson's theorem in bilayer nickelates (arXiv:2512.15023)
[208] Chen C-Q, Qiu W, Luo Z, Wang M and Yao D-X 2026d Electronic structures and superconductivity in nd-doped $La_3Ni_2O_7$ *Sci. China Phys. Mech. Astron.* **69** 247414
[209] Sharma S, Zhao Y-F and Botana A S 2026 Structural stability, electronic structure and magnetic properties of the single-layer trilayer $La_3Ni_2O_7$ polymorph *Phys. Rev. B* **113** 045139
[210] Geisler B, Hamlin J J, Stewart G R, Hennig R G and Hirschfeld P 2026 Electronic reconstruction and interface engineering of emergent spin fluctuations in compressively strained $La_3Ni_2O_7$ on $SrLaAlO_4$(001) *Phys. Rev. B* **113** 054516
[211] Shao Z-Y, Ji J-H, Wu C, Yao D-X and Yang F 2026 Possible liquid-nitrogen-temperature superconductivity driven by perpendicular electric field in the single-bilayer film of $La_3Ni_2O_7$ at ambient pressure *Nat. Commun.* **17** 1120
[212] Oh H, Wu Y-M, May-Mann J, Yu Y, Hwang H Y, Zhang Y-H and Raghu S 2026a High spin, low spin, or gapped spins: Magnetism in the bilayer nickelates *Phys. Rev. B* **113** 024430
[213] Oh H, May-Mann J and Zhang Y-H 2026b Incommensurate pair-density-wave correlations in two-leg ladder t–j–$j_{\perp}$ model (arXiv:2602.04945)
[214] Lange H, Chen A, Georges A, Grusdt F, Bohrdt A and Roth C 2026 Simulating superconductivity in mixed-dimensional $t_{\parallel}$–$j_{\parallel}$–$j_{\perp}$ bilayers with neural quantum states (arXiv:2602.10091)
[215] Wu Y-M, Wang H-X, Smailagić S V, Helbig T and Raghu S 2026b Superconductivity and magnetism in bilayer nickelates: itinerant perspective (arXiv:2602.20288)
[216] Liu H and Khaliullin G 2026 Triplon-mediated pairing and the superconducting gap structure in bilayer nickelates (arXiv:2602.23989)

[217] Watanabe H, Sakakibara H and Kuroki K 2026 Hierarchical structure of primary and hybridization-induced superconducting correlations in bilayer nickelates (arXiv:2603.13604)
[218] Chen Z, Ji J-H, Liu Y-B, Zhang M and Yang F 2026e Filling and interlayer superexchange control superconductivity in $La_3Ni_2O_7$ (arXiv:2603.14519)
[219] Wu H, Zhao Y-F and Botana A S 2026c Pressure and strain tuning of the alternating bilayer-trilayer ruddlesden-popper nickelate: crystal and electronic structure (arXiv:2603.16072)
[220] Zhao J-Y and Zhang Y-H 2026 Pseudogap and non-fermi-liquid criticality in double kondo model for bilayer nickelates (arXiv:2603.25742)
[221] Zhan J, Bejas M, Schnyder A P, Greco A, Wu X and Hu J 2026 Detecting pairing symmetry of bilayer nickelates using electronic raman scattering *Chin. Phys. Lett.* **43** 020706
[222] Wang Y, Wang Z, Zhang F-C and Jiang K 2026f Jahn-teller distortion on strained $La_3Ni_2O_7$ thin films (arXiv:2604.02191)
[223] Cao Y-H, Jiang K-Y, Lu H-Y, Wang D and Wang Q-H 2026b Tunable superconductivity and spin density wave in $La_3Ni_2O_7/LaAlO_3$ thin films (arXiv:2604.05590)
[224] Wei Y, Liu X, Yang F and Jiang M 2026 Perpendicular electric field induced $s^{\pm}$-wave to d-wave superconducting transition in thin film $La_3Ni_2O_7$ (arXiv:2604.07185)
[225] Stepanov E A, Bötzel S, Eremin I M and Lechermann F 2026 Co-operating multiorbital and nonlocal correlations in bilayer nickelate (arXiv:2604.08221)
[226] Wang Z, Jiang K, Zhang F-C and Jin H-K 2026g Orbital-selective d-wave superconductivity in the two-band t–j model: possible applications to $La_3Ni_2O_7$ (arXiv:2604.08319)
[227] Bejas M, Zhan J, Wu X, Schnyder A P and Greco A 2026 Raman response in superconducting multiorbital systems with application to nickelates *Phys. Rev. B* **113** 144504
[228] Li X, Tu W, Lv R, Liu L, Shao D, Sun Y and Lu W 2026d Machine learning accelerated search for superconductors in bcn based compounds and $R_3Ni_2O_7$-type nickelates *Phys. Rev. B* **113** 054521
[229] Zong Y-Y, Yu S-L and Li J-X 2026 Correlation-driven orbital-selective fermiology and superconductivity in the bilayer nickelate $La_3Ni_2O_7$ (arXiv:2605.10101)
[230] Zhou J, Song R and Lu H 2026b Pressure-driven evolution of electronic and magnetic correlations in bilayer nickelate $La_3Ni_2O_7$ (arXiv:2608.02261)
[231] Liu Y-B, Shao Z-Y, Pan Z, Lu C and Yang F 2026d Orbital-selective diagonal-gap test of pairing in $La_3Ni_2O_7$ (arXiv:2606.29470)
[232] Bohrdt A, Homeier L, Reinmoser C, Demler E and Grusdt F 2021 Exploration of doped quantum magnets with ultracold atoms *Ann. Phys.* **435** 168651
[233] Bohrdt A, Homeier L, Bloch I, Demler E and Grusdt F 2022 Strong pairing in mixed-dimensional bilayer antiferromagnetic mott insulators *Nat. Phys.* **18** 651
[234] Hirthe S *et al* 2023 Magnetically mediated hole pairing in fermionic ladders of ultracold atoms *Nature* **613** 463
[235] Schlömer H, Bohrdt A, Pollet L, Schollwöck U and Grusdt F 2023 Robust stripes in the mixed-dimensional t–j model *Phys. Rev. Res.* **5** L022027
[236] Ma T, Wang D and Wu C 2022 Doping-driven antiferromagnetic insulator-superconductor transition: a quantum monte carlo study *Phys. Rev. B* **106** 054510
[237] Scalapino D, Zhang S-C and Hanke W 1998 $so(5)$ symmetric ladder *Phys. Rev. B* **58** 443
[238] Wu C and Zhang S-C 2005 Sufficient condition for absence of the sign problem in the fermionic quantum monte carlo algorithm *Phys. Rev. B* **71** 155115
[239] Wu C, Hu J-P and Zhang S-C 2003 Exact $so(5)$ symmetry in the spin-3/2 fermionic system *Phys. Rev. Lett.* **91** 186402
[240] Capponi S, Wu C and Zhang S-C 2004 Current carrying ground state in a bilayer model of strongly correlated systems *Phys. Rev. B* **70** 220505
[241] Wu C 2006 Hidden symmetry and quantum phases in spin-3/2 cold atomic systems *Mod. Phys. Lett. B* **20** 1707
[242] Kotliar G and Liu J 1988 Superexchange mechanism and d-wave superconductivity *Phys. Rev. B* **38** 5142
[243] Anderson P W 1987b The resonating valence bond state in La_2CuO_4 and superconductivity *Science* **235** 1196
[244] Greenblatt M 1997 Ruddlesden-popper $Ln_n + 1Ni_nO_3n + 1$ nickelates: structure and properties *Curr. Opin. Solid State Mater. Sci.* **2** 174
[245] Nakatsuji S and Maeno Y 2000 Quasi-two-dimensional mott transition system $Ca_{2-x}Sr_xRuO_4$ *Phys. Rev. Lett.* **84** 2666
[246] Georges A, d. Medici L and Mravlje J 2013 Strong correlations from hund's coupling, Annu *Rev. Condens. Matter Phys.* **4** 137
[247] Cava R, Batlogg B, Palstra T, Krajewski J, Peck W Jr, Ramirez A and Rupp L Jr 1991 Magnetic and electrical properties of $La_{2-x}Sr_xNiO_{4+\delta}$ *Phys. Rev. B* **43** 1229
[248] Freeman P, Boothroyd A, Prabhakaran D, Frost C, Enderle M and Hiess A 2005 Spin dynamics of half-doped $La_{3/2}Sr_{1/2}NiO_4$ *Phys. Rev. B* **71** 174412
[249] Anissimova S *et al* 2014 Direct observation of dynamic charge stripes in $La_{2-x}Sr_xNiO_4$ *Nat. Commun.* **5** 3467
[250] Li Z, Guo W, Zhang T T, Song J H, Gao T Y, Gu Z B and Nie Y F 2020 Epitaxial growth and electronic structure of ruddlesden–popper nickelates ($La_n + 1Ni_nO_3n + 1$, $n = 1$–5) *APL Mater.* **8** 091112
[251] Sutter D *et al* 2017 Hallmarks of hunds coupling in the mott insulator Ca_2RuO_4 *Nat. Commun.* **8** 15176
[252] Nakamura F *et al* 2002 From mott insulator to ferromagnetic metal: A pressure study of Ca_2RuO_4 *Phys. Rev. B* **65** 220402(R)
[253] Alireza P L *et al* 2010 Evidence of superconductivity on the border of quasi-2d ferromagnetism in Ca_2RuO_4 at high pressure *J. Phys.: Condens. Matter* **22** 052202
[254] Dietl C *et al* 2018 Tailoring the electronic properties of ca2ruo4 via epitaxial strain *Appl. Phys. Lett.* **112** 031902
[255] Ricco S *et al* 2018 In situ strain tuning of the metal-insulator-transition of ca2ruo4 in angle-resolved photoemission experiments *Nat. Commun.* **9** 4535
[256] Nobukane H *et al* 2020 Co-appearance of superconductivity and ferromagnetism in a Ca_2RuO_4 nanofilm crystal *Sci. Rep.* **10** 3462
[257] Zhu Y *et al* 2024 Superconductivity in pressurized trilayer $La_4Ni_3O_{10-\delta}$ single crystals *Nature* **631** 531
[258] Shi M *et al* 2025c Pressure induced superconductivity in hybrid ruddlesden-popper $La_5Ni_3O_{11}$ single crystals *Nat. Phys.* **21** 1780
[259] Ubbens M U and Lee P A 1994 Spin-gap formation in bilayer cuprates due to enhanced interlayer pairing *Phys. Rev. B* **50** 438